EFFECTS OF CARBON NANOTUBE COATING ON BUBBLE DEPARTURE DIAMETER AND FREQUENCY IN POOL BOILING ON A FLAT, HORIZONTAL HEATER

A Thesis

by

STEPHEN THOMAS GLENN

Submitted to the Office of Graduate Studies of
Texas A&M University
in partial fulfillment of the requirements for the degree of

MASTER OF SCIENCE

August 2009

Major Subject: Mechanical Engineering

EFFECTS OF CARBON NANOTUBE COATING ON BUBBLE DEPARTURE DIAMETER AND FREQUENCY IN POOL BOILING ON A FLAT, HORIZONTAL HEATER

A Thesis

by

STEPHEN THOMAS GLENN

Submitted to the Office of Graduate Studies of
Texas A&M University
in partial fulfillment of the requirements for the degree of

MASTER OF SCIENCE

Approved by:

Chair of Committee,	Debjyoti Banerjee
Committee Members,	Thomas Lalk
	Kamran Entesari
	Frederick Best
Head of Department,	Dennis O'Neal

August 2009

Major Subject: Mechanical Engineering

ABSTRACT

Effects of Carbon Nanotube Coating on Bubble Departure Diameter and Frequency in Pool Boiling on a Flat, Horizontal Heater. (August 2009)

Stephen Thomas Glenn, B.S., Texas A&M University

Chair of Advisory Committee: Dr. Debjyoti Banerjee

The effects of a carbon nanotube (CNT) coating on bubble departure diameter and frequency in pool boiling experiments was investigated and compared to those on a bare silicon wafer. The pool boiling experiments were performed at liquid subcooling of 10°C and 20°C using PF-5060 as the test fluid and at atmospheric pressure. High-speed digital image acquisition techniques were used to perform hydrodynamic measurements.

Boiling curves obtained from the experiments showed that the CNT coating enhanced critical heat flux (CHF) by 63% at 10°C subcooling. The CHF condition was not measured for the CNT sample at 20°C subcooling. Boiling incipience superheat for the CNT-coated surface is shown to be much lower than predicted by Hsu's hypothesis. It is proposed that bubble nucleation occurs within irregularities at the surface of the CNT coating. The irregularities could provide larger cavities than are available between individual nanotubes of the CNT coating.

Measurements from high-speed imaging showed that the average bubble departing from the CNT coating in the nucleate boiling regime (excluding the much larger bubbles observed near CHF) was about 75% smaller (0.26 mm versus 1.01 mm)

and had a departure frequency that was about 70% higher (50.46 Hz versus 30.10 Hz). The reduction in departure diameter is explained as a change in the configuration of the contact line, although further study is required. The increase in frequency is a consequence of the smaller bubbles, which require less time to grow. It is suggested that nucleation site density for the CNT coating must drastically increase to compensate for the smaller departure diameters if the rate of vapor creation is similar to or greater than that of a bare silicon surface.

DEDICATION

This work is dedicated to my family, whose love and support make everything possible.

ACKNOWLEDGEMENTS

I thank my committee chair, Dr. Banerjee, for his patience and guidance throughout the course of this research and for graciously offering the use of his lab. I also thank my committee members, Dr. Lalk, Dr. Best, and Dr. Entesari, for their cooperation and feedback.

Thanks go to my colleagues (and now friends) from the Multi-Phase Flow and Heat Transfer Laboratory at Texas A&M University. Manoj, Rohit, Navdeep, Pratanu, Ranil, Vijay, David, Dominik, Emily, and Matt—I am grateful for your friendship and your willingness to help. Special thanks to Manoj, Rohit, Dominik, Emily, and Matt, who spent many hours aiding me in my research. A very special thanks goes to Vijay, who spent an inordinate amount of time and effort in preparing and running the experiments. The raw data for the bare surface was collected solely by him. His advice and guidance was invaluable and I am lucky to have had such an experienced colleague and friend in the lab.

The University of Texas at Dallas is gratefully acknowledged for synthesizing the carbon nanotube (CNT) coating. Another special thank you is due to Stephen Gauntt for providing me with his Visual Basic program and allowing me to modify it.

Many thanks to the Texas A&M University Graduate Diversity Fellowship for the generous financial assistance. And finally, thanks to my mother and father for their love and support.

NOMENCLATURE

A	surface area (m^2)
Bo	Bond number
c_p	specific heat (J/kg-K)
CF	calibration factor (pixels/mm)
C_g	geometric factor
d_D	departure diameter of bubble (mm)
D_c	critical cavity diameter (m)
D_{cl}	contact line length (m)
f	departure frequency of bubble (1/s)
F_b	buoyancy force (N)
F_s	surface tension force (N)
F_g	force of gravity (N)
g	gravitational acceleration (m/s^2)
h_{fg}	latent heat of vaporization (J/kg)
Ja	Jacob number
Ja^*	modified Jacob number
k	thermal conductivity (W/m-K)
N	nucleation site density ($1/m^2$)
Pr	Prandtl number
q''	heat flux (W/cm^2)

r	radius of cavity (m)
t	elapsed video time (ms)
T_{sat}	saturation temperature (°C)
T_w	wall temperature (°C)
$\dot{V}$	volumetric flow rate of vapor (m^3/s)
y	y-coordinate measurement (pixels)

Greek Symbols

α	thermal diffusivity (m^2/s)
θ	contact angle (degrees)
μ	dynamic viscosity (Pa-s)
ρ	density (kg/m^3)
σ	surface tension (N/m)
ω	uncertainty

Subscripts

l	liquid
v	vapor

TABLE OF CONTENTS

Page

Page

LIST OF FIGURES

Page

Page

Page

Page

LIST OF TABLES

Page

CHAPTER I

INTRODUCTION

Background

There has been a renewal of interest in boiling research over the last decade. With the gradual but consistent decrease in electronic feature sizes on microchips, the heat fluxes required to cool the chips have increased significantly. Currently, fin-fan cooling is the predominant method of heat dissipation, but it is approaching the limit of its practical application. At high heat fluxes, fans and heat sinks would need to be prohibitively large. For this reason, future cooling systems will likely utilize boiling heat transfer to achieve high heat fluxes in compact designs. However, boiling is a complex phenomenon and therefore requires sophisticated modeling and analyses.

Higher heat fluxes are obtained in boiling than in single phase convection for the same temperature differential between source and sink temperatures. This occurs due to combined transport mechanisms involving mass transfer associated with latent heat transfer, sensible heat transfer (by forced or natural convection) as well as periodic transient conduction through direct liquid-solid contact (and contribution from "micro-layer" effects). At high temperatures, radiation heat transfer can also be a significant factor. As the bubbles nucleate and depart from the surface, they absorb energy through the phase change and also promote circulation of colder fluid to the heater surface,

---

This thesis follows the style of ASME Journal of Heat Transfer.

increasing convective heat transfer.

There is still some disagreement as to whether it is the latent thermal energy transfer or the enhanced convective heat transfer due to increased fluid mixing (in combination with transient conduction into the liquid) that plays a larger role in enhancing the boiling heat flux. If latent thermal energy transfer is the dominant mechanism, then it follows that by predicting the volume flow rate of vapor from the surface one may estimate the heat flux at the surface as

$$q'' = \frac{\rho_v \dot{V} h_{fg}}{A} \tag{1}$$

where h_{fg} is the latent heat of vaporization, A is the area of the heater surface, and ρ_v is the vapor density. If we approximate the bubble as a sphere, then the volumetric flow rate of the vapor $\dot{V}$, can be represented by

$$\dot{V} = \frac{\pi}{6} A N d_D^3 f \tag{2}$$

where N is the number of nucleation sites per unit area, d_D is the bubble departure diameter and f is the bubble departure frequency. Thus, there are three important parameters for investigating latent thermal energy transfer: departure diameter, departure frequency, and nucleation site density. If convection enhancement is the dominant mechanism, the departure diameter and frequency would still play a role in quantifying the added mixing of the fluid near the surface.

From prior studies reported in the literature [1-9], various theoretical, empirical, and semi-empirical correlations have been proposed for predicting bubble departure diameter and frequency. However, these correlations show wide variability in their predictions and are applicable to a limited range of operational parameters. Part of the difficulty is in properly accounting for the many experimental parameters and thermo-physical properties that are important in boiling heat transfer. Another problem is the difficulty in achieving repeatable results with which to compare correlations. The experimental data provided in the literature are widely scattered and therefore do not provide very good feedback for evaluating correlations. After evaluating 12 correlations for predicting bubble departure diameter from the literature, Jensen and Memmel [1] concluded that Kutateladze and Gogonin [2] had the best-fitting correlation with an average absolute deviation (AAD) of 45.4%. While their proposed correlation reduced the AAD to 44.4%, it is evident that much work needs to be done to reduce the uncertainty in both the correlations and the experimental data.

In addition to the problems discussed above, existing models now face new challenges. Since Jensen and Memmel's study that was reported in 1986, techniques for the fabrication and characterization of micro- and nano-scale particles and structures have been developed which have been used to modify surfaces and fluids in boiling systems. The effects of these modifications on boiling heat transfer are significantly greater than can be explained by current theory due to the involvement of poorly understood mechanisms at very small length and time scales. One such modification consists of a layer of vertically aligned carbon nanotubes (CNTs) on a silicon substrate.

Carbon nanotubes have high thermal conductivity and mechanical strength. Studies [10-12] of CNT-coated surfaces have shown an increase in the boiling heat transfer coefficient and critical heat flux (CHF), as well as a significant decrease in the boiling incipience superheat. Another modification involves doping refrigerants or solvents with nano-particles. Recently, anomalous experimental data were obtained [13-15] for pool boiling of these nano-particle laden solvents, or nanofluids.

It is not understood exactly how CNT coatings affect the overall heat transfer, although it is generally believed that the CNTs increase the number of nucleation sites to promote heat transfer in the nucleate boiling regime. The greater number of sites would trap more vapor when the system is initially filled with fluid and could explain the lowering of the boiling incipience superheat. Other factors that may be important are lateral capillary flow within the coating (capillary pumping) [16], the fin effect, and transient conduction from the surface to the liquid due to the height of the CNTs [10-11].

Motivation for Study

The long term goal is to develop a theory of boiling heat transfer that better predicts the behavior of systems with nano- and micro-structured surfaces. This theory can then be used to aid in the design of high-heat-flux, two-phase cooling systems for the next generation of electronic chips. A systematic investigation of each mechanism needs to be conducted as shown in Fig. 1 below. Currently, no bubble departure diameter and frequency data exists in the literature for CNT-coated surfaces.

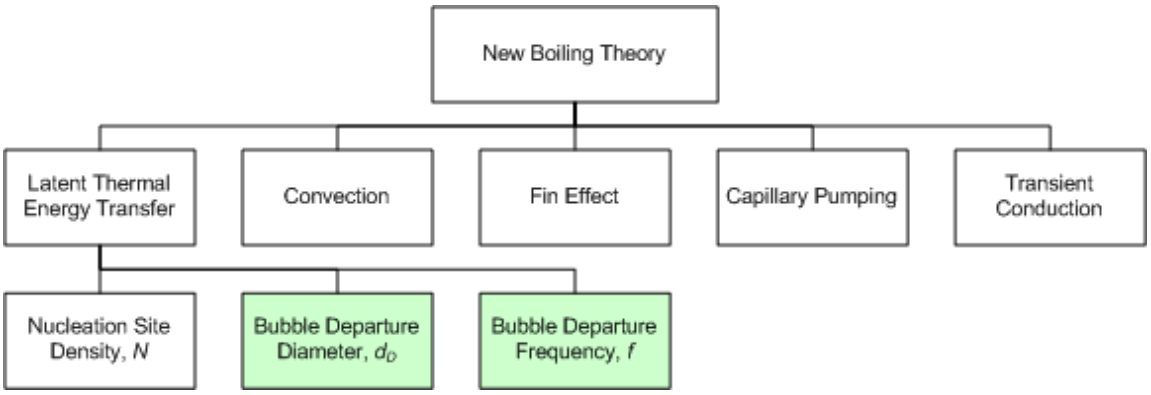

Fig. 1 Research strategy for developing a new boiling theory for micro- and nano-scale surface and fluid modifications with the focus of the present investigation highlighted in green

Objective

The present study is focused on the latent heat transfer mechanism as expressed in Eq. (1) above. From this equation, $\dot{V}$ was the only parameter to be investigated, since ρ_v and h_{fg} are properties of the fluid. This led to the three variables in Eq. (2) that determine $\dot{V}$. The nucleation site density N was left for a future investigation. Therefore, the objective of the present research was to determine the effects of the CNT coating on bubble departure diameter d_D and frequency f.

Scope

Pool boiling experiments were conducted for a bare silicon surface and a CNT-coated silicon surface using PF-5060 at 10°C and 20°C subcooling at atmospheric pressure to measure heat flux at different wall superheats,. The boiling curves produced from the experiments were compared to the literature reports to benchmark the performance of the CNT-coated surface. Two runs for each level of subcooling were

performed for the bare silicon surface to assess the repeatability of the results from the experimental apparatus and procedure. Only one run was performed for the CNT-coated surface at each level of subcooling. Nucleate boiling and film boiling data were taken for the bare silicon surface, but due to problems with the experimental apparatus only nucleate boiling data were taken for the CNT-coated surface. Additional equipment problems prevented measurements near CHF for the CNT-coated surface at 20°C subcooling.

A high-speed video was recorded at each steady state point in the pool boiling experiments. Bubble departure diameter and bubble departure frequency measurements were made using the frames from these videos. The results from the CNT-coated surface were compared to those of the bare surface to determine the effect of the coating on departure diameter and frequency. In the discussion of results, ideas are presented to explain how the CNT coating achieves these effects. The departure diameter results were also compared with correlations from the literature to see if the predictions for the CNT-coated surface were worse than for the bare silicon surface.

Overview

The experimental apparatus and procedure are described in Chapter II. In Chapter III, the uncertainty estimation of the heat flux, departure diameter, and departure frequency are discussed, followed by presentation and discussion of the boiling curves, departure diameter measurements, and departure frequency measurements. The results and conclusions from this study are summarized in Chapter IV. All measurements are

presented in tables in Appendix A. Appendix B provides detailed information on Hsu's hypothesis calculations discussed in Chapter III.

CHAPTER II

EXPERIMENTAL APPARATUS AND PROCEDURE

Apparatus

The system used to conduct the pool boiling experiments is depicted in the schematic in Fig. 2 below and was constructed in 2005 by Dr. Hee Seok Ahn (former Ph.D. student of Mechanical Engineering in the Multi-Phase Flow and Heat Transfer Lab at Texas A&M University). The major components of the system are the viewing chamber, power supply, constant temperature bath, and data acquisition systems.

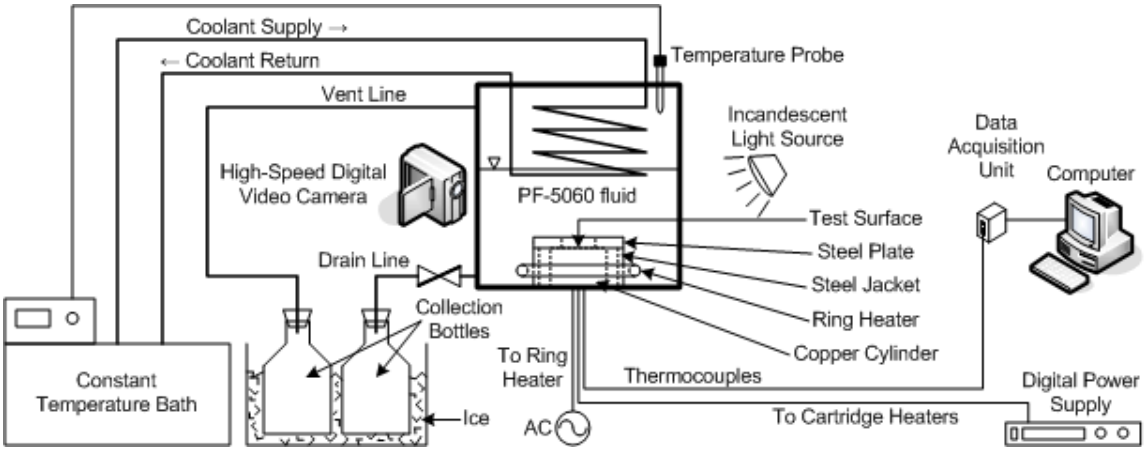

Fig. 2 Experimental apparatus schematic

Viewing Chamber

Three Pyrex glass windows, each sandwiched by silicone rubber gaskets and clamped down by screws and steel plates, allows for viewing of the test samples. At the bottom of the viewing chamber is a copper cylinder heater apparatus which contains 5

cartridge heaters and 12 thermocouples (see Fig. 3). The cylinder is 3.5 in. in diameter and 2.5 in. in height. Four groups of calibrated K-type thermocouples are located inside the cylinder at depths of 0.1250 in., 0.3750 in., 0.6250 in., and 0.8750 in. from the top surface. Each group consists of three thermocouples, with one centrally located and the other two at angular locations of either 0°, 120°, 180°, or 300°. This configuration results in six pairs of vertically-aligned thermocouples, with two of the pairs in the center and the other four at each angular location. The latter are a distance away from the center equal to half the radius of the cylinder. One-dimensional heat conduction to the test surface is promoted by the insulation underneath the chamber and by the air-filled annulus around the copper block created by the steel jacket. The heater surfaces (plain and CNT-coated silicon wafers) were mounted in the viewing chamber on the copper cylinder.

The steel jacket is mounted onto the bottom of the viewing chamber using screws with a silicone rubber gasket in between. The steel plate has a 2.5 in. x 3 in. filleted rectangular opening for the test sample. Before mounting a test sample, a circular Teflon sheet (with the filleted rectangle shape cut out) was glued to the bottom of the steel plate to create a seal with the test sample and to promote heat transfer from the test sample to the fluid rather than through the steel plate. The steel plate was then screwed into the top of the steel jacket with a silicone rubber ring in between.

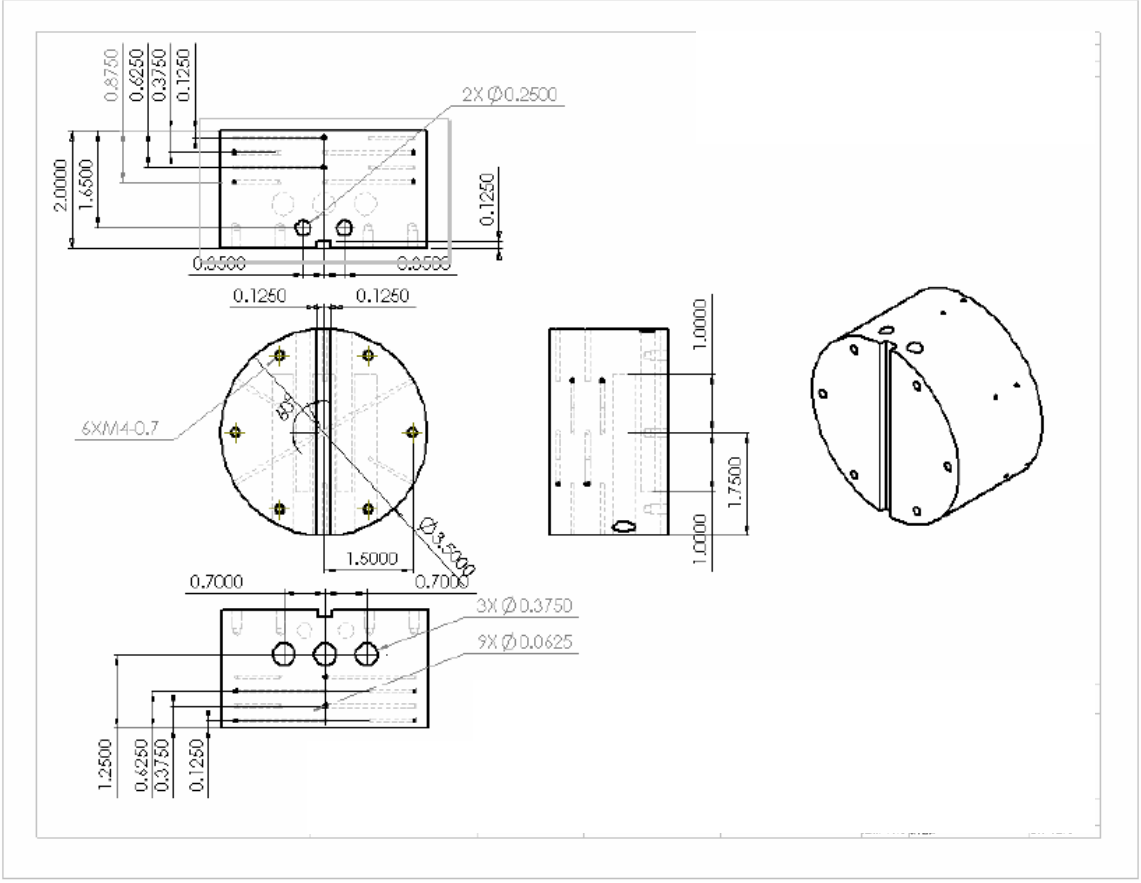

Fig. 3 Schematic of the copper cylinder heater apparatus, units in inches (Image by Sinha [17])

The viewing chamber has a drain line for removing the test fluid and a vent line for maintaining atmospheric pressure inside the viewing chamber. The lid of the viewing chamber provides access for a temperature probe and for coolant fluid supply and return lines, which are used to subcool the liquid in the viewing chamber. The lid also has a port for pouring in the test fluid. Thermocouples are attached to the test surface and also mounted within the liquid pool. Access ports for the vent and drain lines and the leads for the ring heater are located on the side of the viewing chamber. The ring heater is used to quickly bring the test fluid to a boil to remove dissolved gasses so as to improve

the repeatability of the tests. The connecting wires for the cartridge heaters and thermocouples mounted in the copper cylinder pass through a hole in the bottom of the viewing chamber.

Power Supply

The three 300W and two 500W cartridge heaters in the copper cylinder are connected to an American Reliance, Inc. digital power supply. A multi-meter and a clamp-on ammeter are used to measure voltage and current supplied to the heaters, although these measurements were not used. Due to technical problems with the digital power supply, the experiment for the CNT-coated surface at 20°C subcooling was conducted using a Staco Energy Products, Co. 0-140V Variac.

Constant Temperature Bath

A PolyScience Model 9612 constant temperature bath is used to maintain the desired level of subcooling for the liquid. Ethylene glycol is circulated through the cooling coils in the viewing chamber by the bath's internal pump.

Data Acquisition Systems

The data acquisition (DAQ) system for temperature measurement consists of a National Instruments (NI) SCXI-1303 terminal block and a NI PCI-6251 DAQ board. The system digitally samples the voltage signal from the thermocouples and sends these values to a desktop computer. The temperature data is recorded on this computer using LABVIEW software.

A Fastec Imaging Corp. Troubleshooter high-speed video camera with an Infinity Model KC 991260 lens (focus from infinity to 985 mm), an Infinity IF-4 991108 objective (2.33x to 2.91x, 71mm to 64mm working distance), and a Lowel P2-10 Pro-light tungsten halogen lamp was used to obtain high-speed video of the bubbles nucleating on the test surfaces.

Test Samples

Since this research has applications in chip cooling, silicon wafers were selected as the substrate. It is also commonly used in the literature and provides a common basis for benchmarking.

Preparation

One bare silicon wafer and one CNT-coated silicon wafer were prepared. The wafers were 3 in. in diameter, P-type, and had (100) orientation. Both samples were outfitted with thin film thermocouples (TFTs) for surface temperature measurements, shown in Fig. 4 below. The TFTs consisted of chromel and alumel layers 250 nm in height that create 10 junctions near the center of the wafer. While a beaded thermocouple is larger than the superheated liquid layer near the surface, the TFTs were thin enough to remain in this layer and provided a more accurate measurement of the surface (or wall) temperature. Photolithography techniques were used to construct the TFTs as described in [17][1]. The CNTs were synthesized using chemical vapor deposition (CVD) at The University of Texas at Dallas using a 5-nm layer of iron catalyst. The

[1] The help of Vijay Sathyamurthi (student at the Multi-Phase Flow and Heat Transfer Laboratory at Texas A&M University) and Nipun Sinha in fabricating the TFTs is gratefully acknowledged.

substrate was sputter-coated with the metal layers at The University of Texas in Austin, TX[2]. Gaps in the CNT coating were designed to avoid short-circuiting the TFTs.

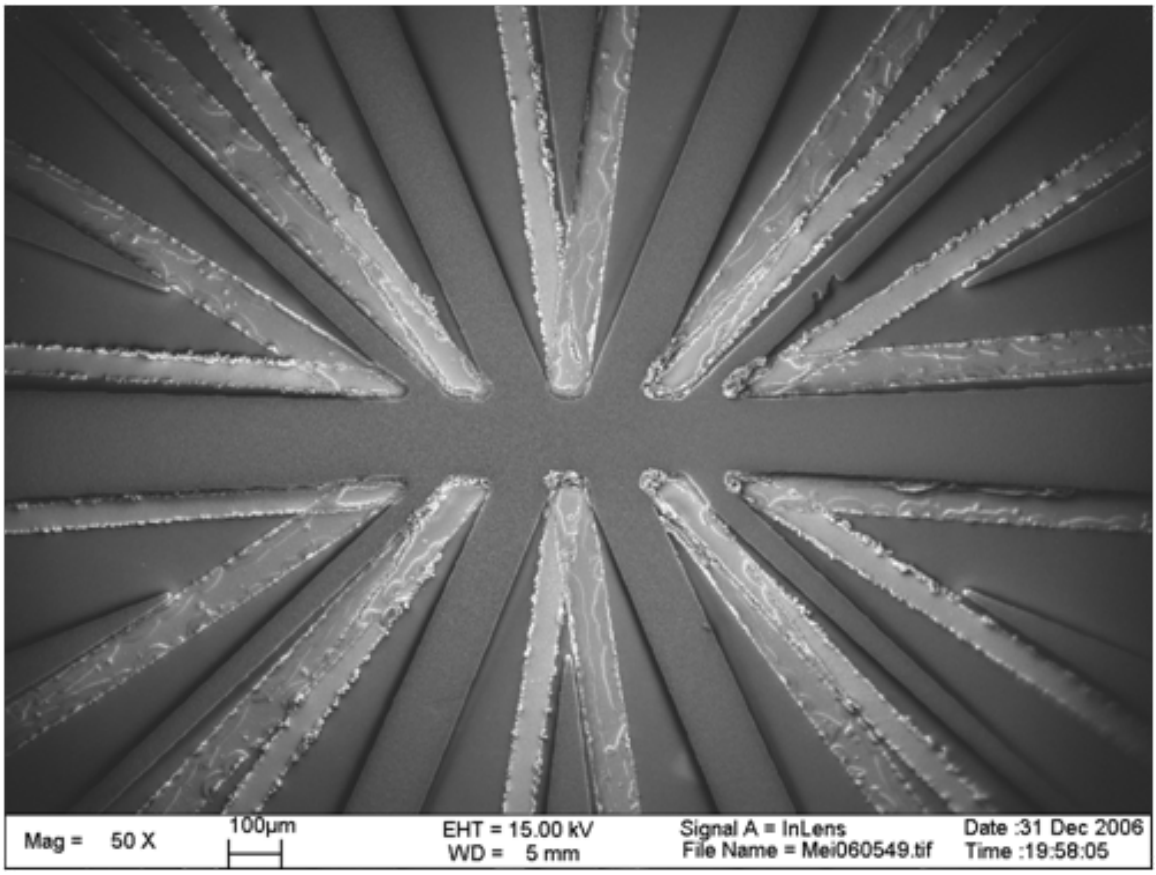

Fig. 4 Scanning electron microscope (SEM) image of the CNT-coated sample showing 10 thin-film thermocouple (TFT) junctions made of chromel and alumel (Image Courtesy of Dr. Mei Zhang, The University of Texas at Dallas)

Characterization

A scanning electron microscope (SEM) was used to measure height and diameter of the CNTs in the coating. The CNTs in the sample were 8-16 nm in diameter and approximately 10-15 μm in height.

[2] The help of Dr. Ray Baughman (The University of Texas at Dallas) and his research group at the Nanotech Institute in synthesizing the CNT coatings is gratefully acknowledged.

Procedure

The procedure for the pool boiling experiments was based on previous studies [10, 11, 18]. The test fluid used was PF-5060, manufactured by 3M, which boils at 56°C at atmospheric pressure. The low boiling point (compared to water) allows higher superheats to be tested without damaging the apparatus, which is required for measuring film boiling conditions. Also, it is a dielectric which is appropriate for electronic chip cooling applications. Subcooled conditions (bulk fluid temperature artificially maintained below saturation temperature) were chosen over saturated conditions since future chip cooling systems are likely to be designed for operation in the subcooled regime.

Before mounting a sample, the top of the copper cylinder was coated with thermal paste, on top of which a Pyrex wafer was placed. The thermal paste reduces interfacial resistance while the Pyrex wafer helps to isolate the thermocouples on the sample from electronic noise originating from the cartridge heaters. Next, another layer of thermal paste was applied to the top of the Pyrex wafer and the sample was placed on top of this layer. Finally, the steel plate (with the Teflon sheet glued to its underside) was mounted to secure the sample.

Before each experiment, the fluid was degassed by vigorously boiling the fluid for 5 minutes using the ring heater. Dissolved gasses in the fluid can affect the repeatability of results by lowering the superheat required to initiate nucleation sites, while increasing the heat flux at a given superheat. The cartridge heaters were not used for degassing since they could initiate nucleation on the surface. Nucleation sites tend to

continue nucleating once they have been activated, so this would adversely affect the repeatability of the results. Once degassing was complete, the ring heater was turned off and the voltage supplied to the cartridge heaters was increased to around 13V. This value, based on previous experiments with the same apparatus, corresponds to a superheat just below the superheat required for boiling inception. The constant temperature bath was then set to maintain the fluid at the appropriate temperature for the test (46°C for 10°C subcooling and 36°C for 20°C subcooling).

Once steady state conditions were achieved (defined as a less than 0.5 °C variation in the copper cylinder temperatures over a period of 5 minutes), data was collected. Temperature measurements were acquired at 200 Hz for approximately 2 minutes, producing about 24000 samples for each thermocouple channel. High-speed video was recorded at 1000 frames per second (fps) at a resolution of 1280 x 511 pixels, with a few exceptions (bare surface, 10°C subcooling, at 10.16°C superheat; CNT-coated surface, 10°C subcooling, at superheats of 22.9°C and 26.5°C) which were recorded at 500 fps at a resolution of 1280 x 1023 pixels to provide a larger field of view. The shutter speed was set between 2 and 10 times the recording rate depending on the amount of light being received by the lens. After reaching steady state, the tungsten halogen lamp would be turned on and the camera would begin recording for about 2 seconds, yielding around 2000 frames for later analysis. The lamp was then immediately turned off to minimize the disturbance to the system in case another video needed to be recorded.

To proceed to the next data point, the voltage to the cartridge heaters was increased by 3V and the constant temperature bath set point was adjusted to maintain the desired level of subcooling. This process was repeated until a stable vapor film was created on the test surface. At this point the voltage was decreased to prevent overheating of the apparatus. Once temperatures within the copper block stabilized at a safe level, the process began again to obtain data for the film boiling regime.

CHAPTER III

RESULTS AND DISCUSSION

Data Reduction and Uncertainty

Boiling Curves

At each steady state condition, the superheat was calculated using temperatures from the TFTs. The heat flux was calculated using Fourier's one-dimensional law of conduction, shown below in Eq. (3), for each of the six pairs of vertically-aligned thermocouples in the heater apparatus.

$$q'' = -k\frac{(T_2 - T_1)}{\Delta x} \tag{3}$$

The values T_1 and T_2 represent measurements from one of the six pairs of thermocouples.

The Kline-McClintock method was used to determine the uncertainty of the heat flux calculations for the boiling curves. The relative uncertainty for each of the six heat flux calculations was calculated using

$$\frac{\omega_{q''}}{q''} = \sqrt{\left(\frac{\omega_k}{k}\right)^2 + \left(\frac{\omega_{T_1}}{T_2 - T_1}\right)^2 + \left(\frac{\omega_{T_2}}{T_2 - T_1}\right)^2 + \left(\frac{\omega_{\Delta x}}{\Delta x}\right)^2} \tag{4}$$

The absolute uncertainty, ω, for each quantity is denoted by a subscript. Thermal conductivity k was taken from standard tables as 401 W/m-K with an uncertainty of

± 1%. The distance between thermocouples in the heater apparatus is represented by Δx and has an estimated uncertainty of ± 3%. The uncertainty of the temperature measurements is the root sum square (RSS) of the precision and bias uncertainties. The bias uncertainty is ± 0.05°C based on the DAQ resolution. The precision uncertainty was taken as a 95% confidence interval of the measurements.

The reported value of the heat flux is an average of the six heat flux calculations at each condition. The root mean square (RMS) was taken of the uncertainty of the heat flux calculations from the six pairs of thermocouples to provide the uncertainty in the average heat flux. The uncertainty of the average heat flux ranges from 0.68 - 0.80 W/cm^2. Uncertainties for the average heat flux calculations are included with the tabulated results in Appendix A.

Departure Diameter

The bubble departure diameter was calculated using

$$d_D = \frac{y_1 - y_2}{CF} \tag{5}$$

where y_1 and y_2 are measured vertical coordinates of the top and bottom of each bubble in pixels and *CF* is the calibration factor associated with the frame resolution. The *CF* for 1280 x 511 and 1280 x 1023 frames was 213.2 pixels/mm and 106 pixels/mm, respectively.

At film boiling conditions, most of the departing bubbles were not completely in frame due to their large size relative to the frame height. To work around this, the visible

portion of the departing bubble was measured and added to the missing upper portion, which was measured in a previous frame. In these cases, the calculation became

$$d_D = \frac{(y_1 - y_2) + (y_3 - y_4)}{CF} \tag{6}$$

The dominant uncertainty for departure diameter measurements originated from the blurry edges of the bubbles in the captured frames. The uncertainty ω_y of the measurements y_1, y_2, y_3, and y_4 was estimated as ± 5 pixels. The Kline-McClintock method was used to derive Eqs. (7) and (8) below from Eqs. (5) and (6), respectively.

$$\omega_{d_D} = \sqrt{2}\frac{\omega_y}{CF} \qquad \text{for 2 measurements} \tag{7}$$

$$\omega_{d_D} = 2\frac{\omega_y}{CF} \qquad \text{for 4 measurements} \tag{8}$$

For the 2-measurement cases (non-film boiling conditions), the uncertainty was ± 0.03 mm and ± 0.07 mm for 1280 x 511 frames and 1280 x 1023 frames, respectively. Most of the non-film boiling conditions were recorded at 1280 x 511 resolution except for bare, subcooled 10°C, Run 1 at 10.2°C wall superheat and CNT, subcooled 10°C at 22.9 °C and 26.5°C wall superheat. For the 4-measurement cases (film boiling conditions), the uncertainty was ± 0.09 mm. All uncertainties for departure diameter are included with the tabulated results in Appendix A.

For further comparisons, groups of departure diameter measurements were averaged. To calculate the uncertainty of these averages, the RSS of the bias and precision uncertainties was taken. The bias was the uncertainty of the samples in the

group (e.g., ± 0.09 mm for film boiling measurements) since there was no precision error component for the samples. If the samples in the group had different uncertainties, an average was taken. The precision error was the 95% confidence interval for the group, which is a function of the standard deviation of the group and the number of samples in the group. The results of these calculations are presented later in this chapter on page 36.

Departure Frequency

Bubble departure frequency (in Hz) was calculated using

$$f = \frac{1000}{t_1 - t_2} \tag{9}$$

where t_1 and t_2 are the elapsed video times (in milliseconds) associated with the departure of consecutive bubbles from the same nucleation site.

The main source of uncertainty in the departure frequency measurements was the temporal resolution of the frames. At 1000 fps (1280 x 511 resolution), each frame is 1 ms apart, while at 500 fps (1280 x 1023 resolution) the frames are 2 ms apart. The uncertainty ω_t was estimated to be half of the temporal resolution (± 0.5 ms and ± 1 ms for 1000 fps and 500 fps, respectively). Equation (10) below was derived using the Kline-McClintock method and was used to calculate the uncertainty in the departure frequency for each measurement.

$$\omega_f = \frac{\sqrt{2\omega_t} f^2}{1000} \tag{10}$$

The uncertainty in the departure frequency ranged from ± 0.03 Hz at 5.85 Hz to ± 14 Hz at 100 Hz. All frequency measurements were made using 1000 fps video except for bare, subcooled 10°C, Run 1 at 10.2°C wall superheat (noted in Table A1 in Appendix A). All uncertainties for departure frequency are included with the tabulated results in Appendix A.

For further comparisons, groups of departure frequency measurements were averaged. To calculate the uncertainty of these averages, the RSS of the bias and precision uncertainties was taken. The bias was the uncertainty of the samples in the group since there was no precision error component for the samples. Since the samples in the group had different uncertainties, an average was taken. The precision error was the 95% confidence interval for the group, which is a function of the standard deviation of the group and the number of samples in the group. The results of these calculations are presented later in this chapter on page 47.

Boiling Curves

Curves showing the variation of heat flux q'' with wall superheat T_w - T_{sat} were created to compare the performance of the CNT-coated surface with the bare surface and with results from the literature. This ensures that the experiments were conducted properly and that the departure diameter and frequency measurements were valid. The results are summarized in Fig. 5. A closer look at the nucleate boiling regime is provided in Fig. 6, while Fig. 7 presents the same data with uncertainty bars.

The heat fluxes at higher subcooling were larger for a given superheat. This is expected since the temperature gradient between the bulk fluid and the superheated fluid at the surface increases with greater subcooling. The increase in boiling heat transfer for CNT-coated surfaces in the fully developed nucleate boiling regime is not as significant as the enhancement in CHF.

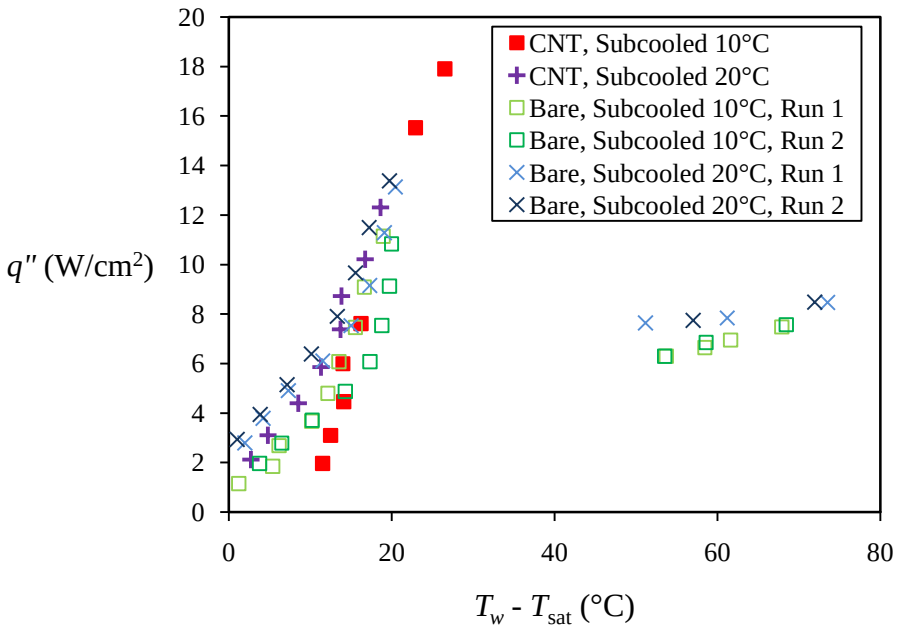

Fig. 5 Boiling curves for all conditions and test runs

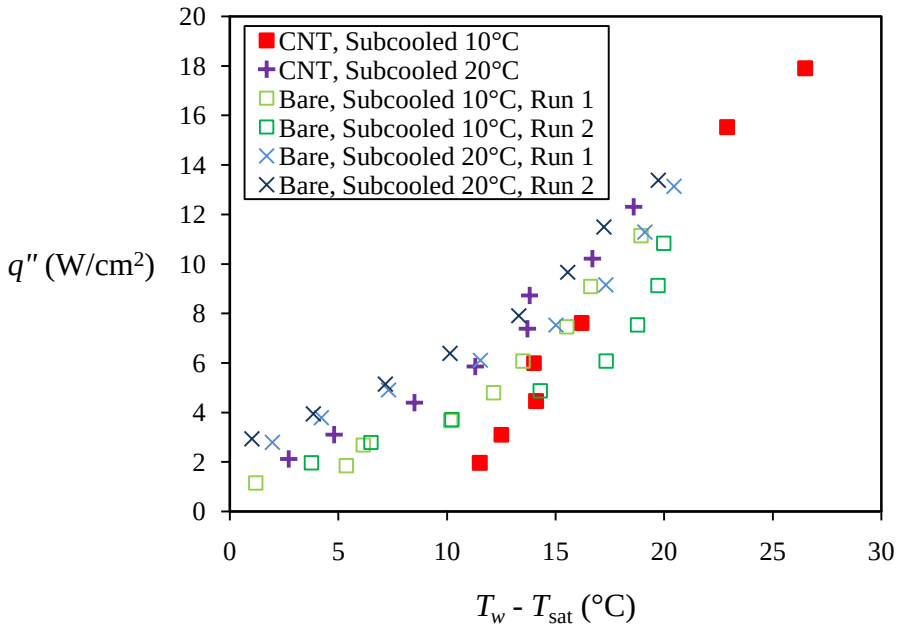

Fig. 6 Boiling curves in the nucleate boiling regime

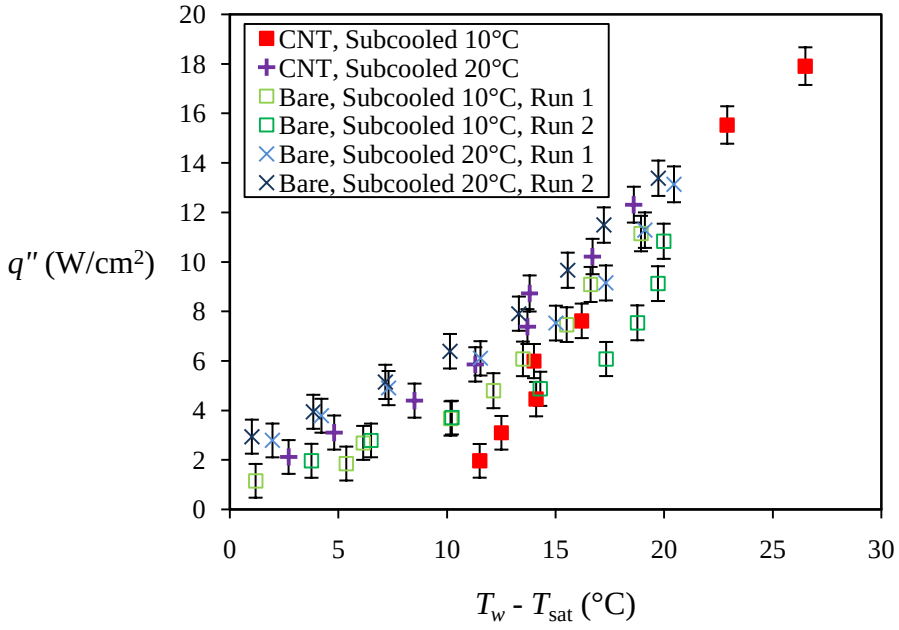

Fig. 7 Boiling curves for the nucleate boiling regime with uncertainty bars

The experiment for the CNT-coated surface at 10°C subcooling had to be stopped after the first five data points due to problems with the power supply and constant temperature bath. The experiment was restarted and measurements were taken at 22.9°C and 26.5°C in reverse order (approaching from the film boiling regime). Data from the film boiling regime and the rest of the nucleate boiling regime were unable to be collected for this second attempt due to continued equipment problems. The critical heat flux condition and film boiling conditions were not reached for the CNT-coated surface at 20°C subcooling due to problems with the constant temperature bath.

There was acceptable repeatability between test runs for the bare silicon surfaces, as shown in Figs. 8 and 9 below, and the results agreed with Sathyamurthi et al. [10].

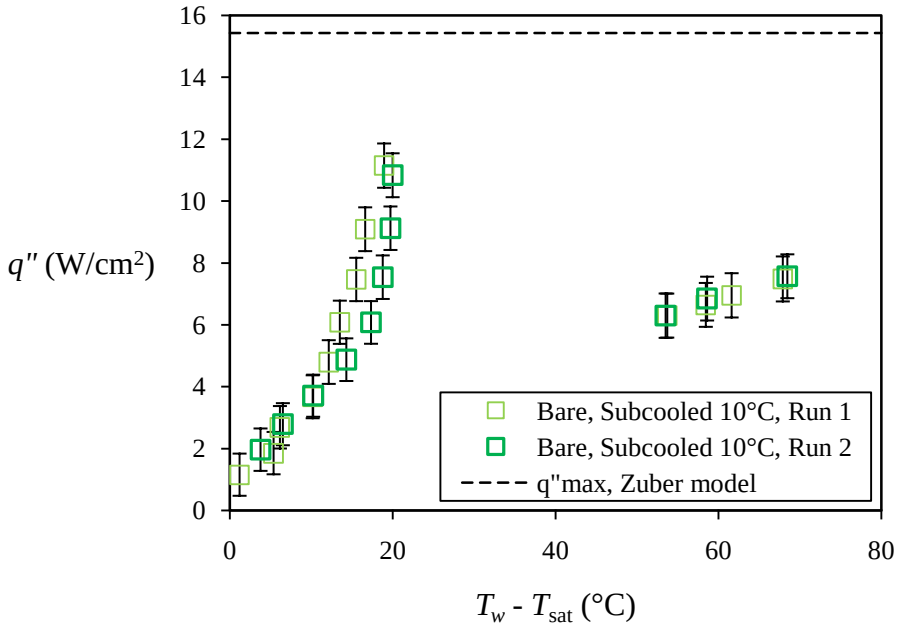

Fig. 8 Boiling curves for bare silicon at 10°C subcooling. The maximum heat flux predicted by Zuber's model is indicated by a horizontal line

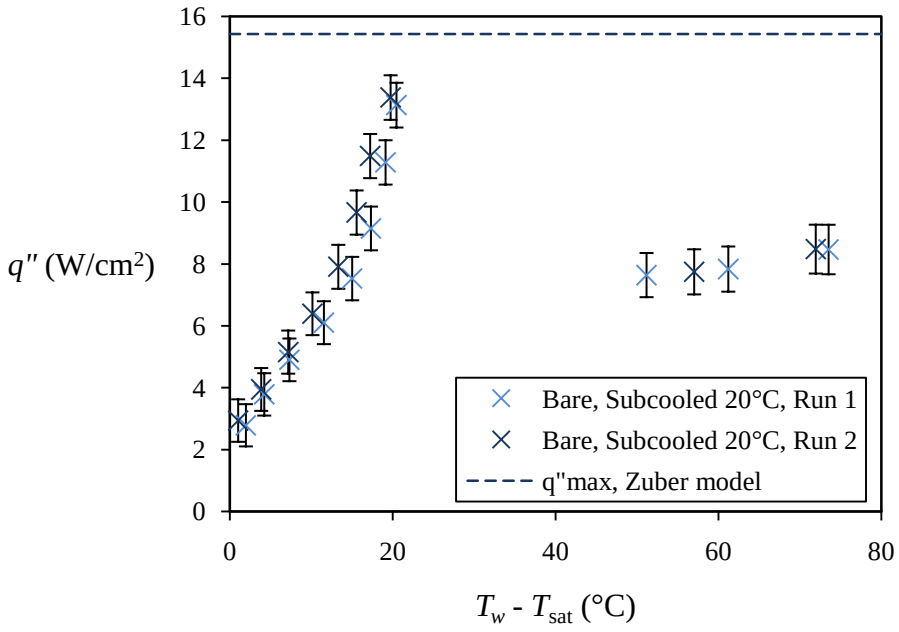

Fig. 9 Boiling curves for bare silicon at 20°C subcooling. The maximum heat flux predicted by Zuber's model is indicated by a horizontal line

The results for the CNT-coated surface tests at 10°C and 20°C subcooling (Fig. 10) show an initially large difference in heat flux that decreases with increasing superheat. The CHF for the CNT-coated surface was 17.9 W/cm^2 ± 4%, which was 13% higher than the CHF reported by Sathyamurthi et al. (15.8 W/cm^2 ± 6%) for a similar surface at the same conditions. The superheat at CHF was 26.5°C while the value reported by Sathyamurthi et al. is 18.6°C. The discrepancy in the CHF points may be due to hysteresis since the CHF point in the present study was approached from the film boiling regime.

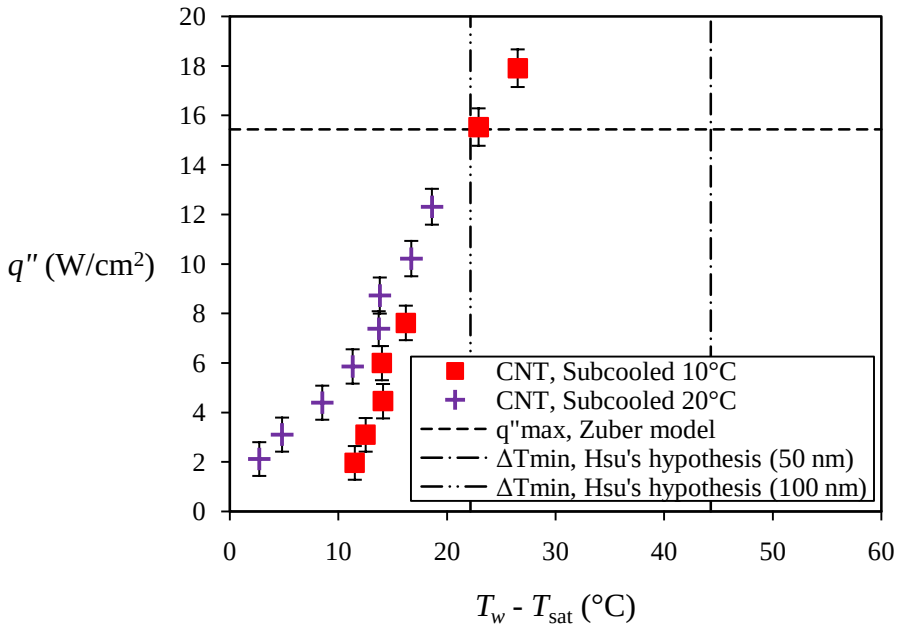

Fig. 10 Boiling curves for the CNT-coated surface with predictions for maximum heat flux and boiling incipience superheat for 50 nm and 100 nm cavity diameters

Comparisons between the test surfaces for a given level of subcooling are provided in Figs.11 and 12 below. At 10°C subcooling, the CNT-coated surface showed an increase in CHF over the bare surface of 61% and 65% (17.9 W/cm^2 versus 10.8 W/cm^2 and 11.1 W/cm^2) for Run 1 and Run 2, respectively. The CNT-coated surface underperformed at low superheat compared to the bare surface. This did not agree with results obtained by Sathyamurthi et al. nor with Ujereh et al. [12], who also showed a reduction in boiling incipience superheat for CNT-coated surfaces compared to bare surfaces. The low superheat region of the boiling curve is more likely to exhibit large variations since initiation of nucleating cavities is highly susceptible to dissolved gases.

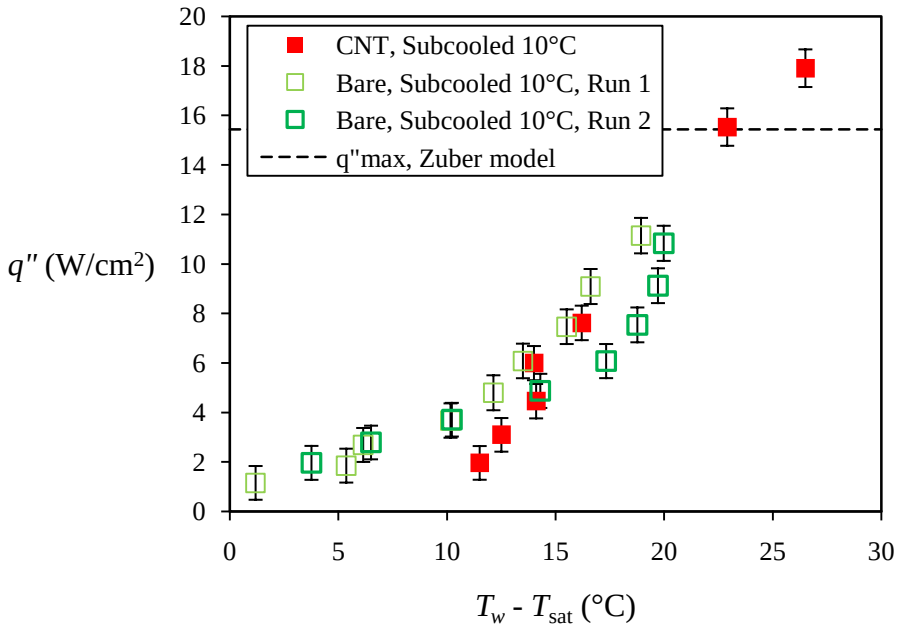

Fig. 11 Comparison of boiling heat flux for CNT-coated and bare surfaces at 10°C subcooling showing an increase in CHF for the CNT-coated surface

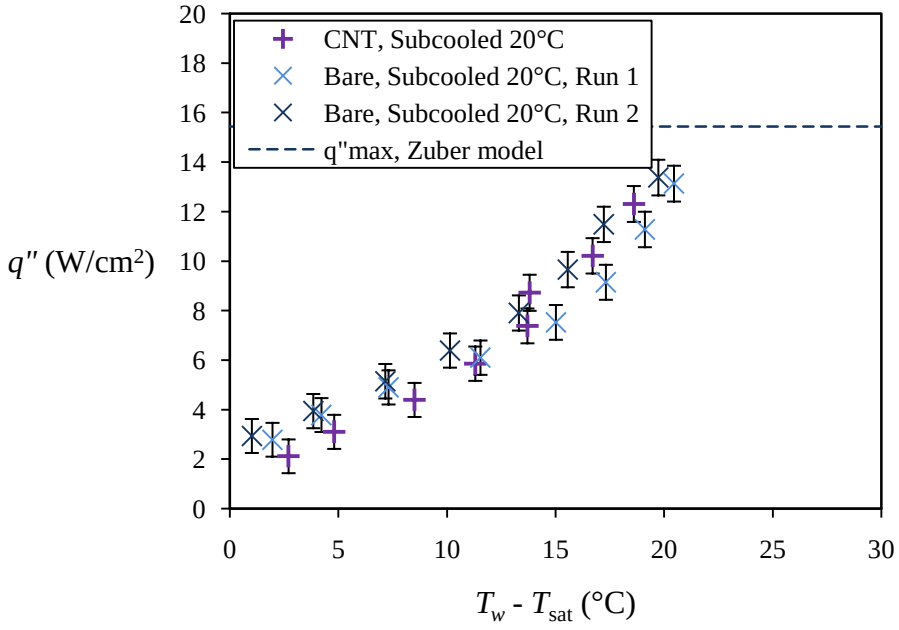

Fig. 12 Comparison of boiling heat flux for CNT-coated and bare surfaces at 20°C subcooling. CHF conditions were not reached for the CNT-coated surface

Zuber's model for maximum heat flux [5] predicts a higher value than was measured for the bare surface experiments, but predicts a lower value than was measured for the CNT-coated surface at 10°C subcooling. CHF conditions were not reached for the CNT-coated surface during the 20°C subcooling experiments so a comparison cannot be made.

The boiling incipience superheat predicted by Hsu's model [19] is based on the nucleating cavity size. Smaller cavities generate smaller nucleating bubbles, which require larger vapor pressures to prevent collapse of the vapor-liquid interface. The pressure that can be achieved in these bubbles is limited by the available wall superheat, which increases the local saturation temperature above that of the bulk liquid. The higher saturation temperature results in a higher saturation pressure within the bubble.

As shown above in Fig. 10, predictions for boiling incipience superheat (44°C for 50 nm cavities and 22°C for 100 nm cavities) significantly overestimate the observed incipience superheats of around 2 and 12°C (see Appendix B for calculations). The values of 50 and 100 nm were chosen based on the pitch of the CNTs within the coating. There are two possible explanations for this discrepancy. One is that the actual cavity size is much larger. Irregularities within the CNT coating or variations in CNT height could provide larger cavities. The second is that the assumption of continuum flow (governed by the Navier-Stokes equations) in Hsu's model is invalid at these length scales.

Considering the first explanation, any entrapped gases in the spaces (<100 nm) between aligned CNTs would likely be driven to the irregularities or to the surface by

capillary action. The Young-Laplace equation, shown in Eq. (11) below, describes the differential pressure achievable for capillary flow in a system given the surface tension σ, the cavity radius *r*, and contact angle θ.

$$\Delta P = \frac{2\sigma}{r}\cos\theta \tag{11}$$

The smaller the cavity radius, the larger the differential pressure available for capillary action (for the same surface and fluid). Therefore the entrapped gases would tend to be driven from the small cavities to the larger cavities. This is consistent with a study by Zhou et al. [20] which shows wicking in a CNT coating—absorbing the fluid throughout the thickness of the coating and displacing any entrapped gases. Thus, the assumption that the nucleating cavities are located within the small gaps in the coating could be wrong.

Scanning electron microscope (SEM) images of the CNT-coated sample are shown in Fig. 13 below. Although the height of the CNT layer did not vary significantly overall, it was observed that in some areas the CNT layer exhibited concentric variations in height ("crop circles") approximately 5-30 μm in diameter. It is not known what causes these irregularities during the synthesis process. Other irregularities observed were along the edges of the CNT coating (in the vicinity of the TFT) and at the surface of the coating where the CNTs are no longer aligned.

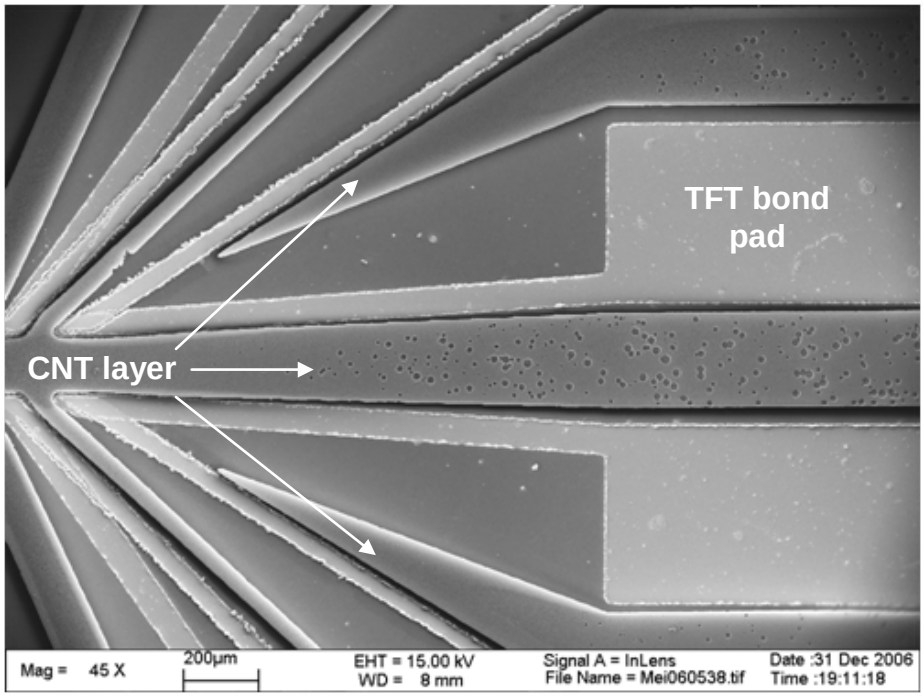

(*a*)

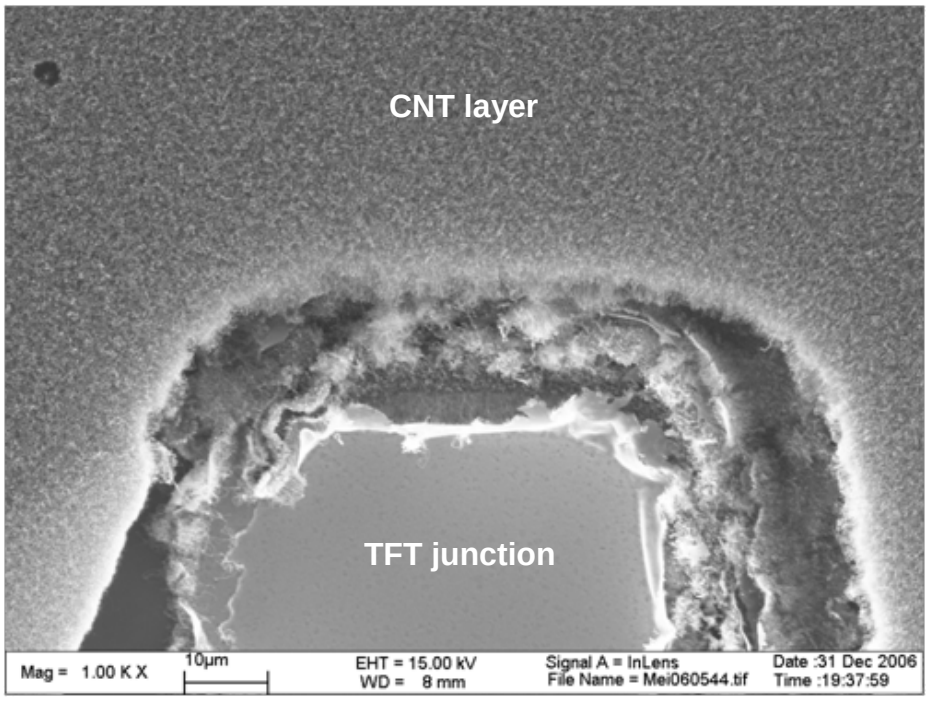

(*b*)

Fig. 13 Scanning electron microscope (SEM) images of the CNT-coated sample (*a*) 4-30 µm "crop circles" in the coating (*b*) irregularities at the edges of the layer as well as near the surface, where the CNTs are not aligned and exhibit variations in height (Images courtesy of Dr. Mei Zhang, University of Texas at Dallas)

Using a 4-μm cavity size with Hsu's model, the boiling incipience superheat is calculated as 0.55°C (see Appendix A for calculation). This value more closely approximates the results (2.7°C for CNT-coated surface at 20°C subcooling).

By considering the previous discussion on wicking, this explanation suggests that entrapped gases are driven to the irregularities in the CNT coating. The larger radius of curvature in these irregularities compared to interstitial cavities means that the nucleation site is less likely to dry out due to the wicking action. Nucleating bubbles in these craters are supplied with fluid from all sides. Colder bulk fluid flows down to the surface as bubbles depart, while fluid from within the CNT coating is drawn to the periphery of the bubble through capillary action. This phenomenon is also described by Macbeth [21] in porous scale deposits and Liter and Kaviany [16] in modulated porous surfaces.

Analysis of Images

After the experiments, high-speed video was split into frames using a MATLAB script. The names of the image files included the frame number as a reference for elapsed video time. A custom VisualBasic® application, based on code by Stephen Gauntt (former M.S. student at the Multi-Phase Flow and Heat Transfer Laboratory at Texas A&M University) and modified by the author, was used to manually measure bubble dimensions in each image on a pixel-based coordinate system. The measurements were recorded into a text file, which were later loaded into a spreadsheet. The calibration

factor for converting the measurements from pixels to millimeters was determined by imaging a ruler on the heater surface. This calibration factor was used within the spreadsheet to provide measurements of bubble departure diameter in millimeters. The frame numbers associated with each measurement are included in the spreadsheet to determine elapsed time in the video frames for the frequency calculation.

Figures 14-17 below provide examples of the high-speed images obtained from the experiments. With the quality of the focus shown, there was some uncertainty in locating the top and bottom of bubbles. However, viewing the images before and after a particular point in time improved the ability to track bubble growth and departure. There was often a range of bubble departure diameters and frequencies in a given video. A best effort was made to take representative samples in these cases.

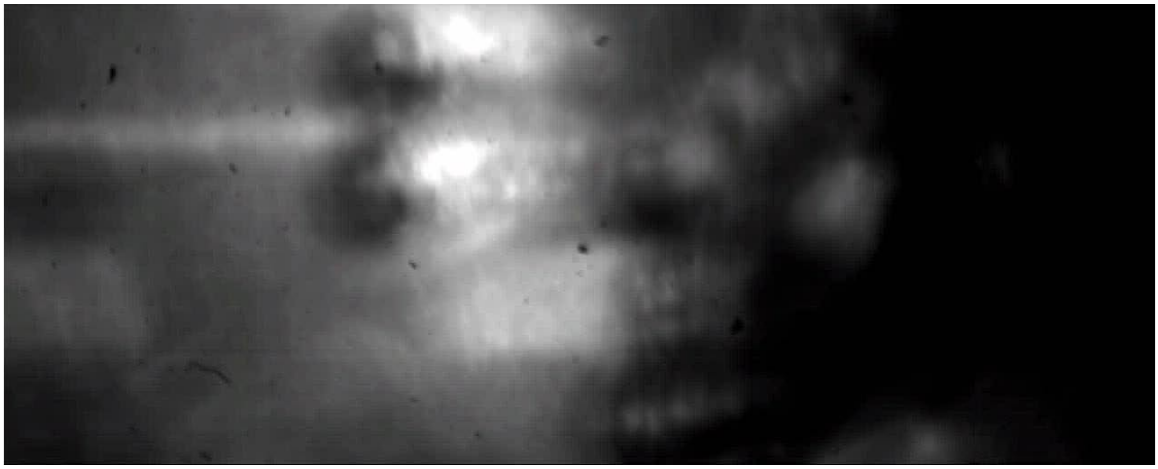

Fig. 14 High-speed image obtained at 10°C subcooling on bare silicon at ~14°C superheat. A bubble and its reflection can be seen slightly left of center. This bubble is on the verge of departing and is approximately 0.8 mm in diameter

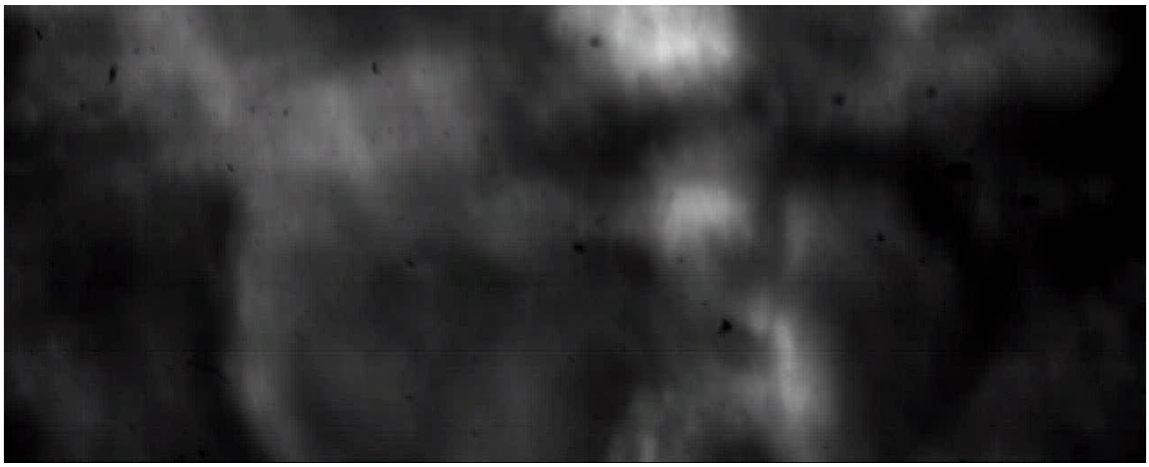

Fig. 15 High-speed image obtained at 20°C subcooling on bare silicon at ~7°C superheat. At top center a bubble can be seen about to depart, measuring ~1 mm

Fig. 16 High-speed image obtained at 10°C subcooling on CNT-coated silicon at ~14°C superheat. Several bubbles measuring ~0.4 mm can be seen near the center of the image

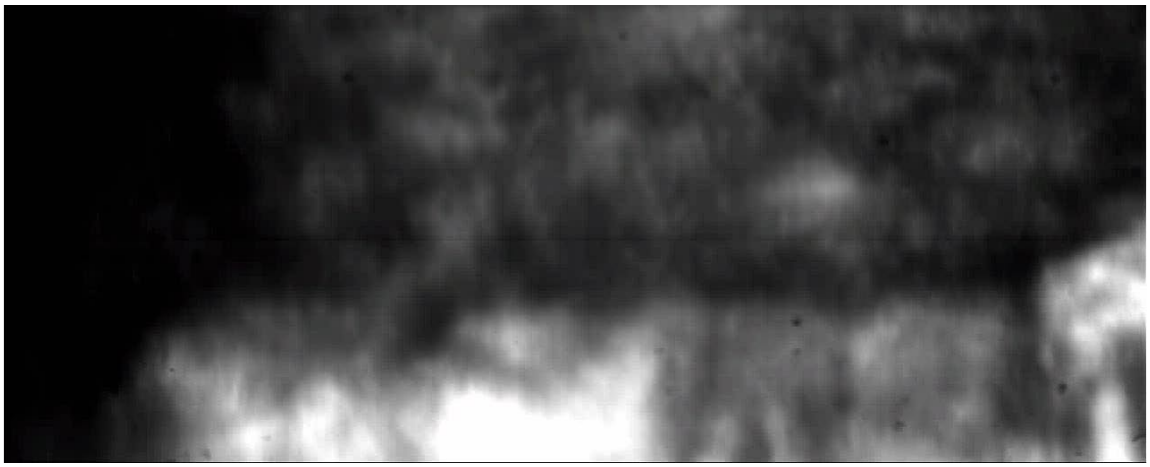

Fig. 17 A wide range of bubble sizes can be seen in this high-speed image taken at 20°C subcooling on CNT-coated silicon at ~14°C superheat. At departure, bubble sizes can range from 0.1 mm to almost 0.6 mm

Departure Diameter

Measurements of bubble departure diameter as they departed were taken for all experiments. The departure diameter was defined to include both the spherical portion of the departing bubble as well as the neck connecting it to the surface. The neck was significant in the film boiling regime, where it accounted for approximately 30% of the total bubble height.

Figure 18 below summarizes the bubble departure diameter measurements for all conditions. A clearer view of the nucleate boiling regime is provided in Fig. 19. As discussed previously, film boiling data for the CNT-coated surface was not obtained due to problems with the experimental apparatus. The figures show significant variation in the measured departure diameters even at low heat superheats, which were easier to observe and had fewer interactions between nucleation sites.

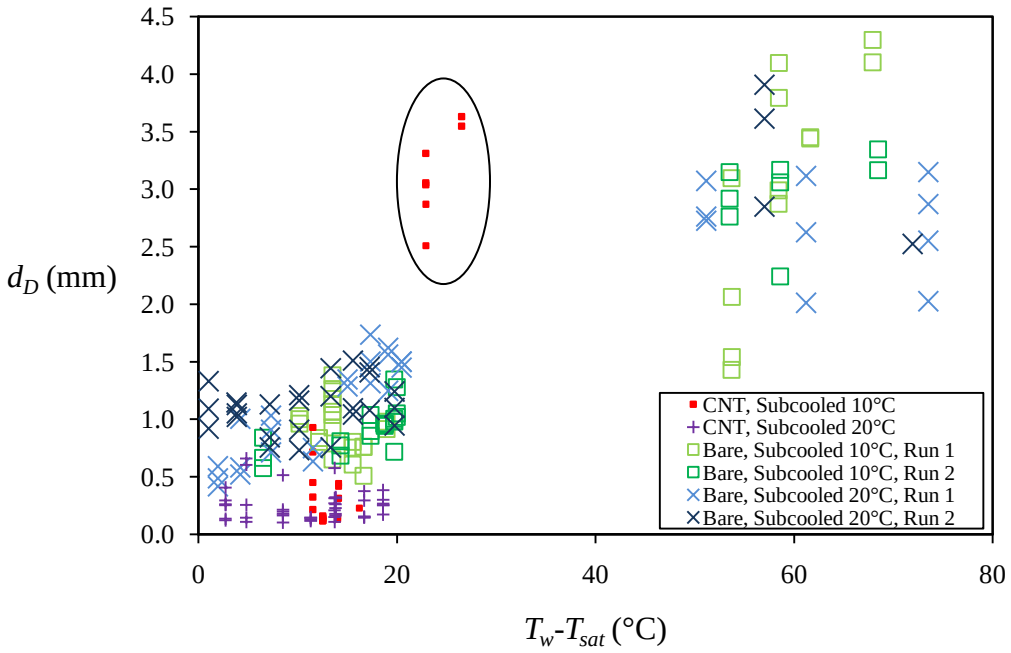

Fig. 18 Variation of bubble departure diameter d_D with wall superheat. The encircled points correspond to CHF approached from the film boiling regime

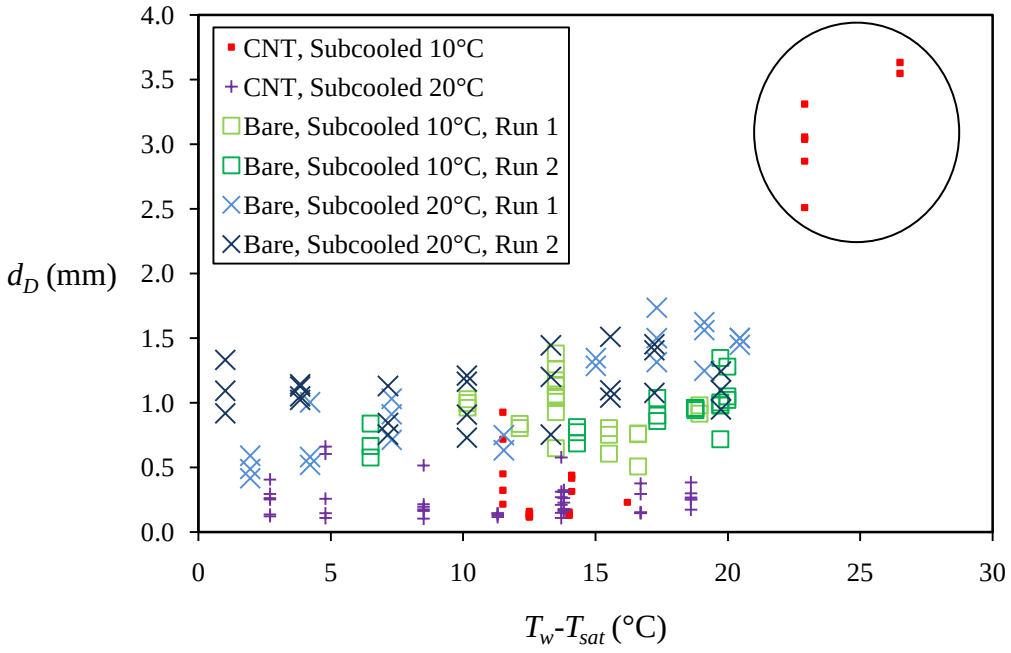

Fig. 19 Variation of d_D with wall superheat in the nucleate boiling regime only. The encircled points were measured approaching from the film boiling regime

Very large bubbles in the range of 2.51-3.63 mm were observed near CHF for the CNT-coated surface at 10°C subcooling. This could be due to the merging of bubbles and could also be due to hysteresis since these data were taken approaching from the film boiling regime. However, it was evident that the CNT-coated surface tended to release significantly smaller bubbles than the plain surface. The CNT-coated surface showed an approximately 75% reduction in departure diameter overall (0.26 mm versus 1.01 mm, excluding the large bubbles near CHF). Table 1 below summarizes the average bubble departure diameters from the experiments.

Table 1 Summary of average bubble departure diameter measurements with absolute uncertainty $\omega_{dD,avg}$

	Average d_D (mm)									
	Bare silicon surface							CNT-coated surface		
	10°C Subcooling			20°C Subcooling				10°C Subcooling	20°C Subcooling	
Regime	Run 1	Run 2	Both	Run 1	Run 2	Both	All			All
Nucleate	0.92	0.92	0.92	1.08	1.10	1.09	1.01	0.28[a]	0.25	0.26[a]
$\omega_{dD,avg}$	0.11	0.09	0.07	0.19	0.09	0.10	0.07	0.11[a]	0.05	0.05[a]
Film	3.10	2.98	3.05	2.69	3.22	2.84	2.96	3.14[b]	-	-
$\omega_{dD,avg}$	0.62	0.30	0.37	0.30	0.90	0.31	0.25	0.36[b]	-	-

[a] Not including the large measurements near CHF
[b] Large measurements near CHF only

The departure diameter averages showed good repeatability between runs at the same conditions although the individual measurements showed significant variation. Different levels of subcooling did not exhibit a change in departure diameter beyond the range of uncertainty.

The following correlations for departure diameter are included in the figures to determine the level of agreement with the data collected. They are listed in terms of the Bond number, which is defined as

$$\mathrm{Bo} = \frac{g d_D^2 \left(\rho_l - \rho_v \right)}{\sigma} \tag{12}$$

1. Ruckenstein [3]:

$$\mathrm{Bo}^{1/2} = \left[\frac{3 \pi^2 \rho_l \alpha_l^2 g^{1/2} \left(\rho_l - \rho_v \right)^{1/2}}{\sigma^{3/2}} \right]^{1/3} \mathrm{Ja}^{4/3} \tag{13}$$

where

$$\mathrm{Ja} = \frac{\rho_l c_{pl} [T_w - T_{\mathrm{sat}}]}{\rho_v h_{fg}} \tag{14}$$

2. Jensen & Memmel [1]:

$$\mathrm{Bo}^{1/2} = 0.19 (1.8 + 10^5 K_1)^{2/3} \tag{15}$$

where

$$K_1 = \left(\frac{\mathrm{Ja}}{\mathrm{Pr}_l} \right)^2 \left\{ \left[\frac{g \rho_l \left(\rho_l - \rho_v \right)}{\mu^2} \right] \left[\frac{\sigma}{g \left(\rho_l - \rho_v \right)} \right]^{3/2} \right\}^{-1} \tag{16}$$

3. Cole [4]:

$$\mathrm{Bo}^{1/2} = 0.04 \mathrm{Ja} \tag{17}$$

where Ja is defined as in Eq. (14).

4. Kutateladze & Gogonin [2]:

$$\mathrm{Bo}^{1/2} = 0.25(1 + 10^5 K_1)^{1/2} \qquad \text{for } K_1 < 0.06 \tag{18}$$

where K_1 is defined as in Eq. (16).

5. Zuber [5]:

$$\mathrm{Bo}^{1/2} = \left[\frac{\sigma}{g(\rho_l - \rho_v)}\right]^{-1/6} \left[\frac{6k_l(T_w - T_{\mathrm{sat}})}{q''}\right]^{1/3} \tag{19}$$

6. Cole & Schulman [6]:

$$\mathrm{Bo}^{1/2} = \frac{1000}{P} \tag{20}$$

where P is pressure in mm Hg.

7. Cole & Rohsenow [7]:

$$\mathrm{Bo}^{1/2} = C(\mathrm{Ja}^*)^{5/4} \qquad \text{for } P_{\mathrm{system}}/P_{\mathrm{critical}} < 0.2 \tag{21}$$

where

$$\mathrm{Ja}^* = \frac{T_{\mathrm{sat}} c_p \rho_l}{\rho_v h_{fg}} \tag{22}$$

and C = 4.65 x 10^{-4}. This value is used for fluids other than water. The units for T_{sat} are Kelvin for Eq. (22) .

8. Fritz [8]:

$$\mathrm{Bo}^{1/2} = 0.0208\theta \tag{23}$$

9. Borishansky & Fokin [9]:

$$\frac{d_D}{d_F} = -\frac{C}{d_F} + \sqrt{\frac{C^2}{d_F^2} + 1} \tag{24}$$

where

$$C = \left(\frac{6}{g}\right)\left(\frac{\rho_l}{\rho_l - \rho_v}\right)\left(\frac{\rho_v}{\rho_l}\right)^{0.4}\left(\frac{q''}{h_{fg}\,\rho_v}\right) \tag{25}$$

and d_F is the diameter calculated from the Fritz correlation (Eq. (23)).

Figures 20 and 21 below show the results for the bare silicon surface at 10°C subcooling for Run 1 and Run 2, respectively. Figures 22 and 23 show the results for the bare silicon surface at 20°C subcooling for Run 1 and Run 2, respectively. A trend of increasing departure diameter with increasing superheat was observed for the bare surface at 10°C subcooling in Run 2 and at 20°C subcooling in Run 1. However, for the other two runs using the bare silicon wafer, the departure diameter did not vary consistently with superheat. There may have existed a bias towards measuring larger bubbles as the number of bubbles in frame increases with increasing superheat.

None of the correlations seemed to agree well with the results. The Cole & Schulman correlation came closest to the measured values for the bare surface, encompassing most of the data within a 50% range. The Cole & Rosenhow correlation matched the lower limits of the experimental data consistently for both runs.

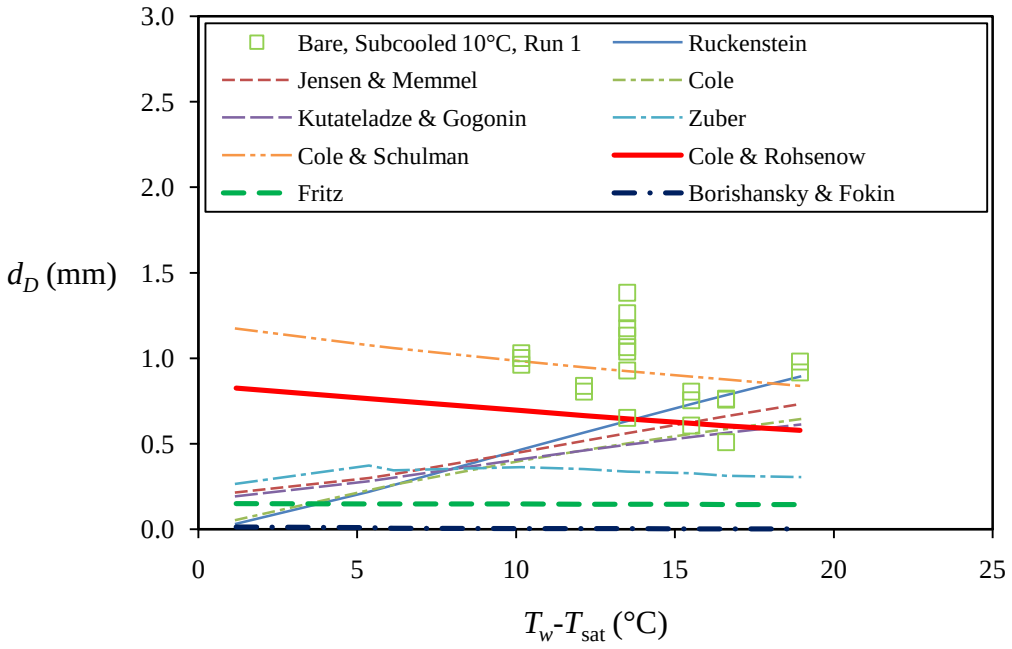

Fig. 20 Comparison of measured departure diameter for the bare surface at 10°C subcooling (Run 1) with predictions from the correlations at these conditions

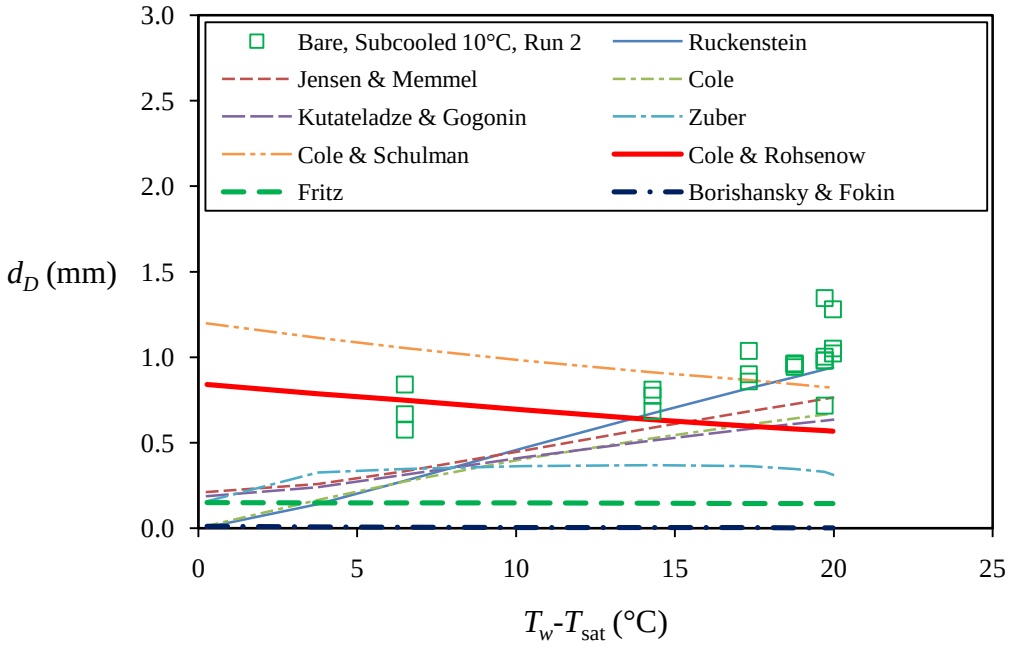

Fig. 21 Comparison of measured departure diameter for the bare surface at 10°C subcooling (Run 2) with predictions from the correlations at these conditions

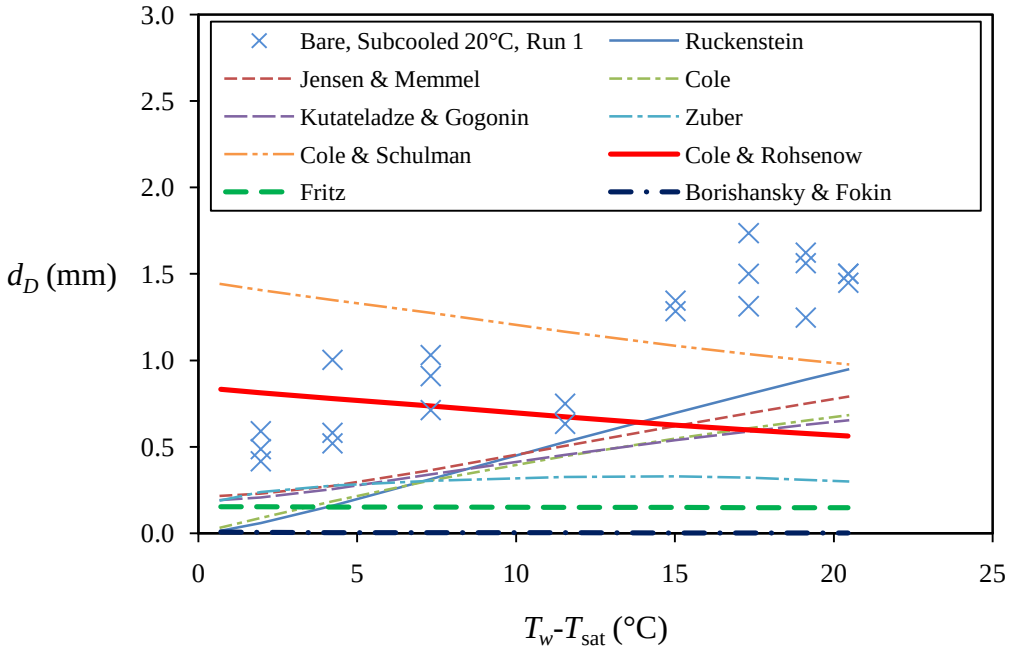

Fig. 22 Comparison of measured departure diameter for the bare surface at 20°C subcooling (Run 1) with predictions from the correlations at these conditions

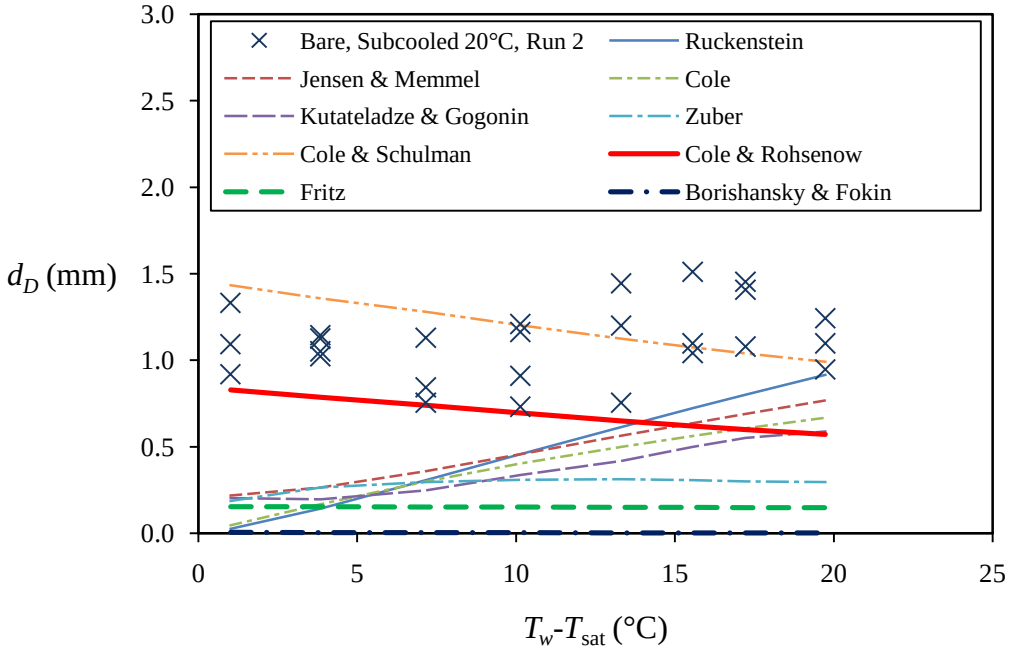

Fig. 23 Comparison of measured departure diameter for the bare surface at 20°C subcooling (Run 2) with predictions from the correlations at these conditions

For the CNT-coated surface, the Fritz and Zuber correlations seemed to fit the best (ignoring the near-CHF data), as shown in Figs. 24 and 25 below. A consistent trend for variation of departure diameter with superheat is not observed from the CNT-coated surface measurements. While the data have some variation, the lower range of the data throughout the range of superheats seems to fall on a boundary at about 0.10 mm. This may indicate that there are smaller bubbles that are not being detected with the techniques used in the present study.

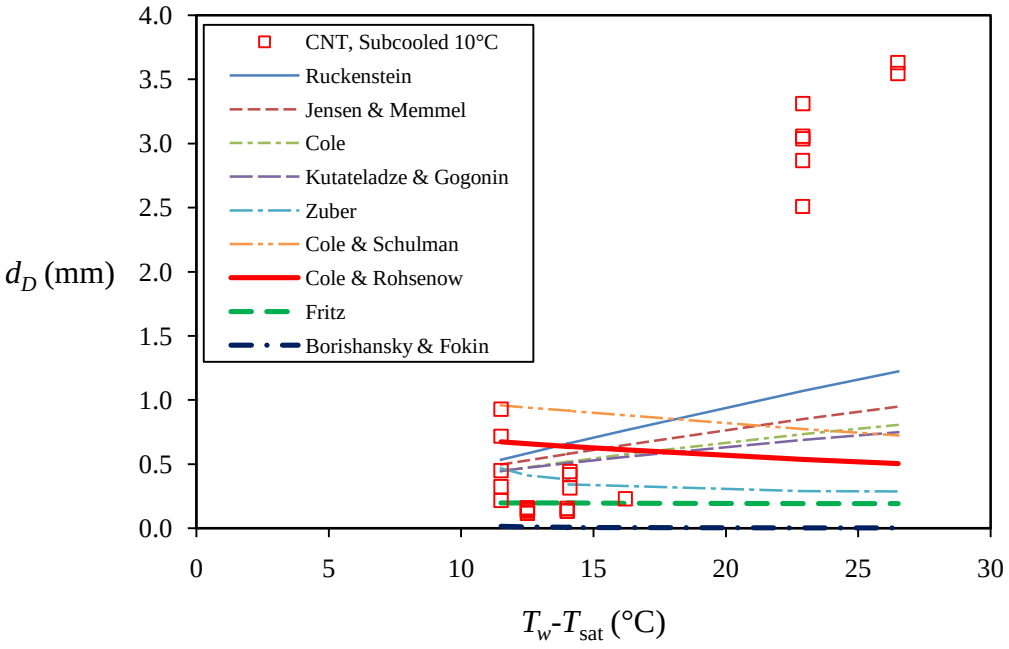

Fig. 24 Comparison of measured departure diameters for the CNT-coated surface at 10°C subcooling with predictions from the correlations

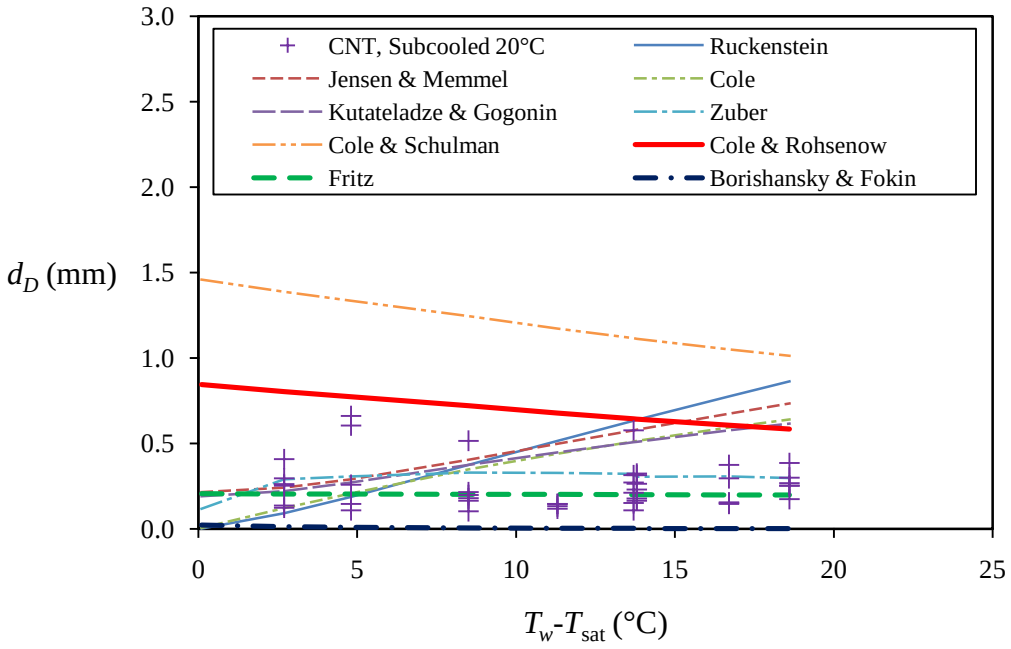

Fig. 25 Comparison of measured departure diameters for the CNT-coated surface at 20°C subcooling with predictions from the correlations

Any agreement with the correlations for the CNT-coated surface data is likely coincidental since none of the correlations predict anything much different for the CNT-coated surface as compared to the bare surface. The fluid properties are used to account for buoyancy, surface, tension, and drag, but the expressions for these forces consist of fluid properties that do not change significantly between test samples. Also, most of the correlations are semi-empirical and were created before CNT-coated heater surfaces were in vogue. Zuber's correlation takes into account the thermal boundary layer, but since the boiling curves for the two samples were similar, this would not produce a significantly different prediction. The only parameter that changes is the contact angle. Sriraman [18] measured the contact angle of PF-5060 on bare silicon and on CNT-coated silicon as 9.65° and 13°, respectively. This is not a large change and it is only

included in Fritz's correlation. Additional terms need to be added to the correlations before any of them would be able to predict bubble departure diameters for a CNT-coated surface.

The smaller departure diameters for the CNT-coated surface can be explained by considering the forces acting on the bubble. At the point of departure, the buoyant force equals or exceeds the surface tension and gravitational forces on the bubble as depicted in Fig. 26 below. Inertial force and drag will be ignored to simplify the discussion. With these simplifications, the forces will be balanced at the point of bubble departure.

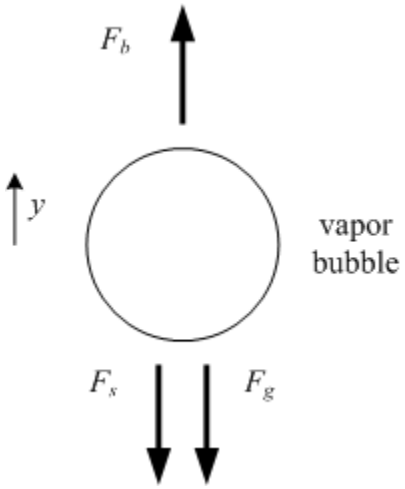

Fig. 26 Free-body diagram of bubble, showing buoyancy force F_b, surface tension force F_s, and the force of gravity F_g, for a bubble about to depart

The buoyant force F_b and gravitational force F_g on a spherical vapor bubble are given by

$$F_b = \frac{\pi}{6} g \rho_l d_D^3 \tag{26}$$

$$F_g = \frac{\pi}{6} g \rho_v d_D^3 \tag{27}$$

The surface tension force F_s is expressed as

$$F_s = C_g \sigma D_{cl} \tag{28}$$

where σ is the surface tension, D_{cl} is the length of the three-phase contact line (where the vapor-liquid interface meets the surface), and C_g is a geometric factor ensuring that only the vertical component of the force is taken into account. From these forces, the following equation is produced

$$F_b - F_g = F_s \tag{29}$$

$$\frac{\pi}{6} g (\rho_l - \rho_v) d_D^3 = C_g \sigma d_D \tag{30}$$

Ignoring small changes in the values of the fluid properties, the only variables affected from one test surface to the other are d_D, C_g, and D_{cl}. Therefore, a change in C_g and D_{cl} could explain the change in d_D observed for the CNT-coated surface.

A CNT-coated surface would have a more complicated the contact line configuration than for plain surfaces. Due to the liquid layer below the bubble and the porous structure of the coating, the conventional single contact line on a plain surface would be modified. The vapor-liquid interface would need to traverse the gaps between

nanotubes, which would create contact lines for each nanotube it is in contact with. There would also be three-phase interfaces below the bubble that do not exist on non-porous surfaces. In addition, the varied directions of the surface tension forces along the many contact lines would affect the value of C_g. This change in C_g could be much more significant than the change in contact angle. All these factors could result in a lower surface tension force F_s and explain the smaller departure diameters observed with the addition of the CNT coating. Further modeling and experimentation is required to determine the effects of CNT coatings on the geometric factor C_g and contact line D_{cl}.

Departure Frequency

The departure frequency was defined as the time between the consecutive departure of two bubbles from the same site. While only a few clear frames are needed to take a departure diameter measurement, a much longer series of clear frames is required to measure departure frequency. Due to the increased difficulty of these measurements, fewer data points for departure frequency were obtained than for departure diameter. High-speed video analysis for the CNT-coated surface at 20°C subcooling failed to produce any frequency measurements. Shown in Fig. 27 below are the frequency data from all experiments. Figure 28 below shows the same frequency data with the addition of uncertainty bars. Since the uncertainty ω_f is proportional to the square of the frequency, the uncertainty bars for frequencies below 55Hz were small enough to be removed for clarity. Averages of the departure frequency measurements are provided in Table 2 below.

Table 2 Summary of average bubble departure frequency measurements with absolute uncertainty $\omega_{f,avg}$

	Average f (Hz)									
	Bare silicon surface							CNT-coated surface		
	10°C Subcooling			20°C Subcooling				10°C Subcooling	20°C Subcooling	
Regime	Run 1	Run 2	Both	Run 1	Run 2	Both	All			All
Nucleate	38.16	34.95	36.23	24.51	18.55	22.43	30.10	50.5[a]	-	-
$\omega_{f,avg}$	16.41	11.15	8.82	7.30	7.02	5.16	5.70	14.3[a]	-	-

[a] Not including the large measurements near CHF

The uncertainty was higher for the average departure frequency results than for the average departure diameter results for two reasons. First, fewer data points were obtained (55 measurements for frequency versus 193 for departure diameter) due to the increased difficulty of the measurements. Second, the scatter was relatively larger than for the departure diameter data (standard deviation ranged from 7.8 to 23 Hz). However, even with the high uncertainty the data still showed that bubble departure frequency for the CNT-coated surface was higher than the average frequency for plain surfaces. Further investigation with more sharply focused images is required to determine if this is true over a larger set of measurements. The increase in frequency for the CNT-coated surface was likely due to the decrease in departure diameter, since less time would be required for the smaller bubbles to reach departure size.

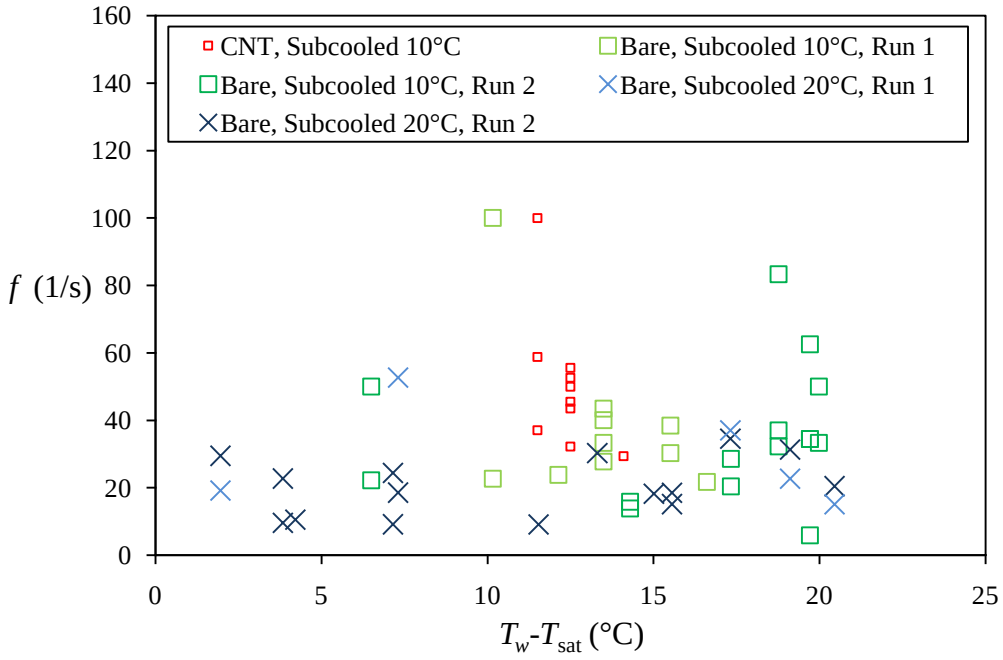

Fig. 27 Variation of measured bubble departure frequency with wall superheat in the nucleate boiling regime

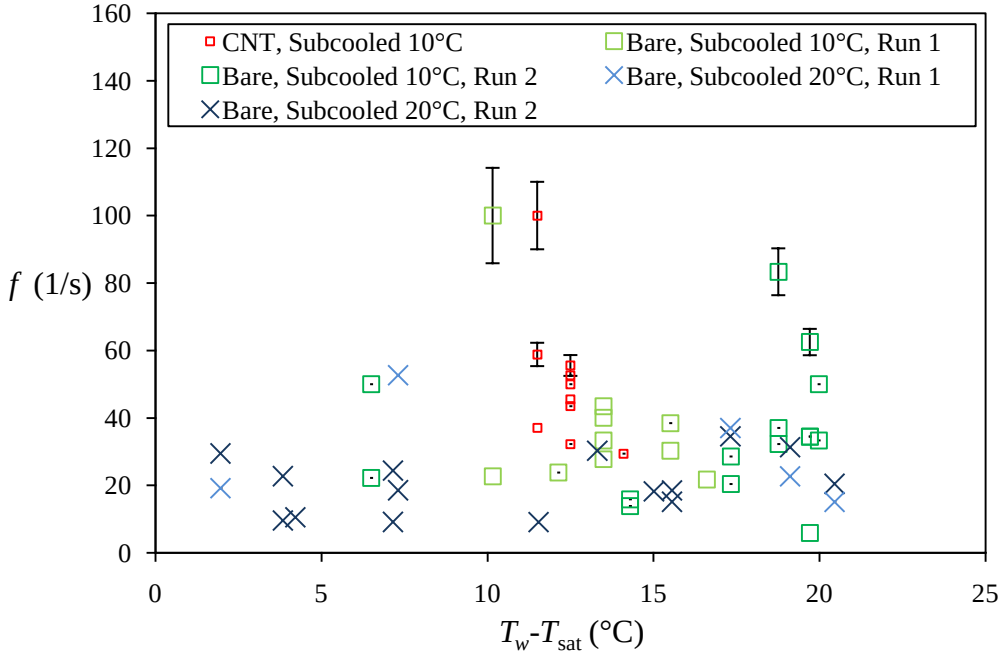

Fig. 28 Variation of bubble departure frequency with superheat in the nucleate boiling regime with uncertainty bars for frequencies greater than or equal to 55 s^{-1}

The data presented in this work showed that the CNT coating enhanced departure frequency (70%) by the same amount as the decrease in the average departure diameter (75%). Since the vapor volumetric flow rate varies with the cube of the departure diameter, these results suggest that the nucleation site density must increase by about 3700% to maintain the same latent thermal energy transfer rate. Sathyamurthi et al. [10] observed an increase in nucleation site density in their CNT-coated sample compared to a bare surface, but did not quantify the change. The estimated maximum nucleation site density (using the inverse square of the average departure diameters measured in the present study) is about 15 sites per mm^2 for the CNT-coated surface and about 1 site per mm^2 for the bare surface. This is not enough of an increase in N to compensate for the effects of the CNT coating on departure diameter and frequency.

CHAPTER IV

SUMMARY AND CONCLUSION

Summary of Results

The effects of a carbon nanotube (CNT) coating on bubble departure diameter and frequency was investigated. Pool boiling experiments were performed for bare and CNT-coated silicon wafers using PF-5060 at atmospheric pressure. Both surfaces were tested in the nucleate boiling regime at 10°C and 20°C subcooling. Additional film boiling data was obtained for the bare silicon sample. High-speed video at 500-1000 frames per second (fps) was used to measure bubble departure diameter and bubble departure frequency for each steady state heat flux condition.

Boiling curves obtained from the experiments showed that critical heat flux (CHF) was enhanced by 63% on the surface with CNT compared to the bare surface at the same wall superheat. Higher subcooling resulted in higher heat flux for both surfaces at the same wall superheat. At 10°C subcooling, the CNT-coated surface initially underperformed at lower superheat compared to the bare surface. However, higher heat flux was obtained from the CNT-coated surface at CHF compared to the bare surface. At 20°C subcooling, the CNT-coated surface initially underperformed at lower superheat compared to the bare surface. Due to problems with the experimental apparatus, CHF conditions could not be obtained on the CNT-coated surface for 20°C subcooling. Boiling incipience superheat was shown to be much lower than predicted by Hsu's model applied to cavity sizes corresponding to the nano-porous coating.

High-speed video measurements showed that the CNT coating reduced bubble departure diameter by about 75% (0.26 mm versus 1.01 mm) and increased frequency by about 70% (50.46 s^{-1} versus 30.10 s^{-1}). These results suggested that the nucleation site density must increase drastically if the same level of latent thermal energy transfer is to be maintained. The diameter was not significantly affected by different levels of subcooling. Correlations in the literature for predicting the departure diameter did not agree well with the results for the CNT coated surface and did not predict a significant change in the departure diameter for the CNT-coated surface compared to a bare surface. Predictions from a few of the correlations (e.g., Cole and Rosenhow; and Cole and Schulman) were found to be consistent with the observed departure diameters for experiments performed on a bare silicon surface.

Possible Mechanisms for CNT Coating Effects

It is proposed that nucleation occurs within irregularities (variations in CNT coating thicknesses) on the surface and at the edges of the CNT coating and not within the gaps between the aligned nanotubes. The spacing between the aligned nanotubes is not expected to serve as nucleation sites since the capillary pressure would drive any gases towards larger spaces near the surface of the coating. Additionally, such small nucleation sites would require a much higher wall superheat to sustain the nucleating bubble. Irregularities in CNT coating thickness (termed “crop circles”) were observed on the CNT-coated sample and are estimated to be approximately 4-30 μm in diameter. Using this value, the minimum wall superheat for nucleation is expected to be 0.5°C

based on Hsu's hypothesis. For nucleation between individual nanotubes, Hsu's hypothesis predicts a boiling incipience superheat of about 44°C based on a cavity size of 100 nm. Hence, the experimental results suggest that nucleation does not occur within the CNT coating but rather on the top surface. Capillary action within the coating may drive the trapped gases towards these craters when the fluid is initially introduced.

Based on a simple force balance, it was proposed that the reduction in departure diameter was caused by a change in the configuration of the contact line. The non-aligned, tangled ends of the CNTs at the surface of the coating would create a complex interface with a nucleating bubble. Rather than one contact line (as in the case of a plain surface), there would be multiple contact lines with a variety of orientations. It is expected that the overall surface force is lower for bubbles nucleating on a CNT coating. This would lower the net buoyancy force required for the bubble to depart and therefore lower the departure diameter. The increase in frequency was likely due to the smaller bubbles, which require less time to grow to departure size.

Future Directions

Future studies could try to determine where nucleation occurs for CNT coatings. This will help to identify potential mechanisms for explaining the effects of the CNT coating. Further investigation is required to see if irregularities such as crop circles are typical for CNT coatings and if they are uniformly distributed.

Quantification of the effect of the CNT coating on nucleation site density is needed. Combined with measurements from the present study and additional departure

frequency measurements, an estimate of the heat flux due to latent thermal energy transfer can be made. This can be compared to the measured overall heat flux to determine the importance of this mechanism relative to all others.

Finally, further studies are required to determine the effect of CNT coatings on both static and dynamic contact line configurations. This will help to explain the decrease in bubble departure diameter on the CNT coating.

REFERENCES

[1] Jensen, M. K., and Memmel, G. J., 1986, "Evaluation of Bubble Departure Diameter Correlations," *Proc. Eighth International Heat Transfer Conference*, C. Tien, V. P. Carey, and J. K. Ferrell, eds., Hemisphere Publishing Corp., Washington, DC, **4,** pp. 1907-1912.

[2] Kutateladze, S. S., and Gogonin, I. I., 1979, "Growth Rate and Detachment Diameter of a Vapor Bubble in Free Convection Boiling of a Saturated Liquid," High Temperature, **17,** pp. 667-671.

[3] Ruckensteitn, E., 1963, "Physical Model for Nucleate Boiling Heat Transfer from a Horizontal Surface," Bul Institutului Politech Bucaresti, **33**(3), pp. 79-88.

[4] Cole, R., 1967, "Bubble Frequencies and Departure Volumes at Subatmospheric Pressures," AIChE J, **13**, pp. 779-783.

[5] Zuber, N., 1959, "Hydrodynamic Aspects of Boiling Heat Transfer," Ph.D. dissertation, University of California - Los Angeles, Los Angeles, CA.

[6] Cole, R., and Shulman, H. L., 1966, "Bubble Departure Diameters at Subatmospheric Pressures," Chem Eng Prog Symp Ser, **62**(64), pp. 6-16.

[7] Cole, R., and Rohsenow, W. M., 1968, "Correlation of Bubble Departure Diameters for Boiling of Saturated Liquids," Chem Eng Prog Symp Ser, **65**(92), pp. 211-213.

[8] Fritz, W., 1935, "Berechnung des Maximalvolume von Dampflblasen," Phys Z, **36**, pp. 379-388.

[9] Borishansky, V. M., and Fokin, F. S., 1963, "Heat Transfer and Hydrodynamics in Steam Generators," Trudy TsKTI, **62**, p. 1.

[10] Sathyamurthi, V., Ahn, H. S., Banerjee, D., and Lau, S.C., 2009, "Subcooled Pool Boiling Experiments on Horizontal Heaters Coated with Carbon Nanotubes," J. Heat Transfer, **131**, 071501.

[11] Ahn, H-S., Sinha, N., Zhang, M., Banerjee, D., Fang, S., Baughman, R., 2006, "Pool Boiling Experiments on Multiwalled Carbon Nanotube (MWCNT) Forests," J. Heat Transfer, **128**(12), pp. 1335-1342.

[12] Ujereh, S., Fisher, T., and Mudawar, I., 2007, "Effects of Carbon Nanotube Arrays on Nucleate Pool Boiling," Int. J. Heat Mass Transfer, **50**(19-20), pp. 4023-4038.

[13] Wang, X., and Mujumdar, A., 2007, "Heat Transfer Characteristics of Nanofluids: A Review," Int. J. Thermal Sciences, **46**(1), pp. 1-19.

[14] Keblinski, P., Eastman, J. A., and Cahill, D. G., 2005, "Nanofluids for Thermal Transport," Materials Today, **8**(6), pp. 36-44.

[15] Nelson, I. C., Banerjee, D., and Ponnappan, R., 2008, "Flow Loop Experiments Using Polyalphaolefin Nanofluids," J. Thermophysics Heat Transfer (2009, in press); DOI 10.2514/1.31033.

[16] Liter, S. G, and Kaviany, M., 2001, "Pool-Boiling CHF Enhancement by Modulated Porous-Layer Coating: Theory and Experiment," Int. J. Heat Mass Transfer, **44**, pp. 4287-4311.

[17] Sinha, N., 2006, "Design, Fabrication, Packaging and Testing of Thin Film Thermocouples for Boiling Studies," M.S. thesis, Texas A&M University, College Station, TX.

[18] Sriraman, S. R., and Banerjee, D., 2008, "Pool Boiling Studies on Nano-Structured Surfaces," *ASME Int Mech Eng Congress Expos Proc*, ASME, New York, NY, **8A**, pp. 317-324.

[19] Hsu, Y. Y., 1962, "On the Size and Range of Active Nucleation Cavities on a Heating Surface," J. Heat Transfer, **84**, pp. 207-213.

[20] Zhou, J. J., Noca, F., and Gharib, M., 2006, "Flow Conveying and Diagnosis with Carbon Nanotube Arrays," Nanotechnology, **17**, pp. 4845-4853.

[21] Macbeth, R. V., 1971, "Boiling on Surfaces Overlayed with a Porous Deposit: Heat Transfer Rates Obtainable by Capillary Action," Atomic Energy Establishment Winfrith Report R.711, United Kingdom Atomic Energy Authority, Chilton, United Kingdom.

APPENDIX A

Table A1 Variation of heat flux, departure diameter, and departure frequency with superheat for bare silicon at 10°C subcooling (Run 1)

Superheat	Heat flux	Absolute uncertainty	Departure diameter	Absolute uncertainty	Departure frequency	Absolute uncertainty
T_w - T_{sat}	q''	$\omega_{q''}$	d_D	ω_{dD}	f	ω_f
°C	W/cm^2	W/cm^2	mm	mm	1/s	1/s
1.2	1.15	0.68	-	-	-	-
5.4	1.85	0.68	-	-	-	-
6.1	2.68	0.69	-	-	-	-
10.2[a]	3.67	0.69	0.96	0.07	100	14
			1.03	0.07	22.7	0.7
			1.00	0.07		
12.1	4.79	0.71	0.80	0.03	23.8	0.6
			0.84	0.03		
13.5	6.08	0.70	1.17	0.03	27.8	0.8
			1.26	0.03	40.0	1.6
			1.38	0.03	33.3	1.1
			0.65	0.03	43.5	1.9
			1.13	0.03		
			0.93	0.03		
			1.07	0.03		
			1.04	0.03		
15.5	7.46	0.70	0.61	0.03	38.5	1.5
			0.75	0.03	30.3	0.9
			0.80	0.03		
16.6	9.09	0.71	0.76	0.03	21.7	0.5
			0.51	0.03		
			0.76	0.03		
18.9	11.14	0.72	0.92	0.03	-	-
			0.98	0.03		
53.7	6.29	0.71	2.06	0.09	-	-
			1.54	0.09		
			3.09	0.09		
			1.43	0.09		
58.4	6.64	0.71	3.79	0.09	-	-
			4.10	0.09		
			2.99	0.09		
			2.87	0.09		
61.6	6.95	0.72	3.44	0.09	-	-
			3.45	0.09		
67.9	7.48	0.73	4.10	0.09	-	-
			4.30	0.09		
	Average (Nucleate boiling)		0.92	0.11	38.2	16.4
	Average (Film boiling)		3.10	0.62	-	

[a] d_D and f measured from 1280 x 1023 video recorded at 500 frames per second

Table A2 Variation of heat flux, departure diameter, and departure frequency with superheat for bare silicon at 10°C subcooling (Run 2)

Superheat	Heat flux	Absolute uncertainty	Departure diameter	Absolute uncertainty	Departure frequency	Absolute uncertainty
T_w - T_{sat}	q''	$\omega_{q''}$	d_D	ω_{dD}	f	ω_f
°C	W/cm^2	W/cm^2	mm	mm	1/s	1/s
0.3	1.28	0.69	-	-	-	-
3.8	1.96	0.68	-	-	-	-
6.5	2.78	0.68	0.84	0.03	50.0	2.5
			0.58	0.03	22.2	0.5
			0.67	0.03		
10.2	3.71	0.69	-	-	-	-
14.3	4.87	0.69	0.77	0.03	15.9	0.3
			0.81	0.03	13.9	0.2
			0.68	0.03		
17.3	6.07	0.70	1.04	0.03	28.6	0.8
			0.90	0.03	20.4	0.4
			0.86	0.03		
18.8	7.54	0.70	0.96	0.03	32.3	1.0
			0.96	0.03	37.0	1.4
			0.94	0.03	83.3	6.9
			0.96	0.03		
19.7	9.12	0.71	1.35	0.03	5.85	0.03
			0.72	0.03	34.5	1.2
			1.00	0.03	34.5	1.2
			0.98	0.03	62.5	3.9
20.0	10.83	0.72	1.05	0.03	33.3	1.1
			1.28	0.03	50.0	2.5
			1.02	0.03		
53.5	6.29	0.71	3.15	0.09	-	-
			2.76	0.09		
			2.92	0.09		
58.6	6.84	0.71	3.17	0.09	-	-
			2.24	0.09		
			3.06	0.09		
68.5	7.57	0.71	3.34	0.09	-	-
			3.17	0.09		
Average (Nucleate boiling)			0.92	0.09	34.9	11.2
Average (Film boiling)			2.98	0.30	-	

Table A3 Variation of heat flux, departure diameter, and departure frequency with superheat for bare silicon at 20°C subcooling (Run 1)

Superheat	Heat flux	Absolute uncertainty	Departure diameter	Absolute uncertainty	Departure frequency	Absolute uncertainty
T_w - T_{sat}	q''	$\omega_{q''}$	d_D	ω_{dD}	f	ω_f
°C	W/cm^2	W/cm^2	mm	mm	1/s	1/s
0.7[a]	1.97	0.68	-	-	-	-
2.0	2.78	0.68	0.42	0.03	29.4	0.9
			0.49	0.03	19.2	0.4
			0.59	0.03		
4.2	3.78	0.68	0.58	0.03	10.5	0.1
			1.00	0.03		
			0.52	0.03		
7.3	4.90	0.69	1.03	0.03	18.5	0.3
			0.91	0.03	52.6	2.8
			0.71	0.03		
11.5	6.10	0.69	0.63	0.03	9.1	0.1
			0.75	0.03		
15.0	7.52	0.70	1.35	0.03	18.2	0.3
			1.29	0.03		
17.3	9.14	0.71	1.50	0.03	34.5	1.2
			1.31	0.03	37.0	1.4
			1.74	0.03		
19.1	11.28	0.72	1.56	0.03	31.3	1.0
			1.62	0.03	22.7	0.5
			1.25	0.03		
20.4	13.13	0.72	1.45	0.03	20.4	0.4
			1.50	0.03	15.2	0.2
			1.50	0.03		
51.2	7.64	0.71	2.73	0.09	-	-
			2.76	0.09		
			3.07	0.09		
61.2	7.83	0.73	2.01	0.09	-	-
			2.63	0.09		
			3.11	0.09		
73.5	8.46	0.80	2.03	0.09	-	-
			2.87	0.09		
			2.55	0.09		
			3.15	0.09		
Average (Nucleate boiling)			1.08	0.19	24.5	7.3
Average (Film boiling)			2.69	0.30	-	

[a] Measurements for this condition were excluded

Table A4 Variation of heat flux, departure diameter, and departure frequency with superheat for bare silicon at 20°C subcooling (Run 2)

Superheat	Heat flux	Absolute uncertainty	Departure diameter	Absolute uncertainty	Departure frequency	Absolute uncertainty
T_w - T_{sat}	q''	$\omega_{q''}$	d_D	ω_{dD}	f	ω_f
°C	W/cm^2	W/cm^2	mm	mm	1/s	1/s
-1.5[a]	2.09	0.69	-	-	-	-
1.0	2.94	0.69	0.92	0.03	-	-
			1.33	0.03		
			1.09	0.03		
3.8	3.94	0.69	1.05	0.03	9.6	0.1
			1.02	0.03	22.7	0.5
			1.13	0.03		
			1.14	0.03		
7.2	5.15	0.70	0.76	0.03	9.2	0.1
			1.13	0.03	24.4	0.6
			0.84	0.03		
10.1	6.39	0.69	0.73	0.03	-	-
			1.16	0.03		
			1.21	0.03		
			0.91	0.03		
13.3	7.91	0.71	0.76	0.03	30.3	0.9
			1.20	0.03		
			1.44	0.03		
15.6	9.66	0.71	1.04	0.03	15.2	0.2
			1.10	0.03	18.5	0.3
			1.51	0.03		
17.2	11.48	0.71	1.08	0.03	-	-
			1.45	0.03		
			1.41	0.03		
19.7	13.38	0.72	1.10	0.03	-	-
			1.24	0.03		
			0.95	0.03		
57.0	7.74	0.73	3.91	0.09	-	-
			3.61	0.09		
			2.85	0.09		
71.9	8.48	0.79	2.52	0.09	-	-
	Average (Nucleate boiling)		1.10	0.09	18.6	7.0
	Average (Film boiling)		3.22	0.90	-	

[a] Measurements for this condition were excluded

Table A5 Variation of heat flux, departure diameter, and departure frequency with superheat for CNT-coated silicon at 10°C subcooling

Superheat	Heat flux	Absolute uncertainty	Departure diameter	Absolute uncertainty	Departure frequency	Absolute uncertainty
$T_w - T_{sat}$	q''	$\omega_{q''}$	d_D	ω_{dD}	f	ω_f
°C	W/cm^2	W/cm^2	mm	mm	1/s	1/s
2.3[a]	-0.41	0.69	0.29	0.03	16.4	0.3
			0.23	0.03	17.5	0.3
			0.23	0.03		
6.5[a]	0.13	0.67	0.38	0.03	20.8	0.4
			0.35	0.03	25.6	0.7
			0.38	0.03		
13.0[a]	0.92	0.67	0.33	0.03	125	16
			0.39	0.03	90.9	8.3
			0.41	0.03	111	12
					100	10
					100	10
					83.3	6.9
11.5	1.96	0.68	0.72	0.03	37.0	1.4
			0.93	0.03	58.8	3.5
			0.22	0.03	100	10
			0.45	0.03		
			0.32	0.03		
12.5	3.09	0.68	0.12	0.03	45.5	2.1
			0.14	0.03	50.0	2.5
			0.15	0.03	55.6	3.1
			0.16	0.03	52.6	2.8
			0.12	0.03	43.5	1.9
			0.14	0.03	32.3	1.0
			0.12	0.03		
14.1	4.45	0.69	0.31	0.03	29.4	0.9
			0.42	0.03		
			0.44	0.03		
14.0	5.99	0.69	0.15	0.03	-	-
			0.13	0.03		
			0.14	0.03		
16.2	7.62	0.70	0.23	0.03	-	-
22.9[abc]	15.53	0.76	2.51	0.09	-	-
			2.87	0.09		
			3.31	0.09		
			3.04	0.09		
			3.06	0.09		
26.5[abc]	17.90	0.76	3.63	0.09	-	-
			3.55	0.09		
	Average (Nucleate boiling)		0.28	0.11	50.5	14.3
	Average (Near CHF)		3.14	0.36	-	

[a] Measurements for this condition were excluded

[b] Near CHF conditions were approached from the film boiling side of the boiling curve

[c] d_D and f measured from 1280 x 1023 video recorded at 500 frames per second

Table A6 Variation of heat flux, departure diameter, and departure frequency with superheat for CNT-coated silicon at 20°C subcooling

Superheat	Heat flux	Absolute uncertainty	Departure diameter	Absolute uncertainty	Departure frequency	Absolute uncertainty
T_w - T_{sat}	q''	$\omega_{q''}$	d_D	ω_{dD}	f	ω_f
°C	W/cm^2	W/cm^2	mm	mm	1/s	1/s
-4.1[a]	0.47	0.70	0.15	0.03	-	-
			0.14	0.03		
			0.23	0.03		
			0.19	0.03		
			0.15	0.03		
			0.15	0.03		
0.1[a]	1.18	0.68	0.33	0.03	-	-
			0.19	0.03		
			0.20	0.03		
			0.20	0.03		
			0.11	0.03		
			0.22	0.03		
2.7	2.12	0.68	0.25	0.03	-	-
			0.14	0.03		
			0.30	0.03		
			0.12	0.03		
			0.26	0.03		
			0.41	0.03		
4.8	3.10	0.69	0.11	0.03	-	-
			0.66	0.03		
			0.61	0.03		
			0.15	0.03		
			0.26	0.03		
8.5	4.39	0.69	0.20	0.03	-	-
			0.52	0.03		
			0.18	0.03		
			0.16	0.03		
			0.10	0.03		
			0.22	0.03		
11.3	5.86	0.69	0.13	0.03	-	-
			0.15	0.03		
			0.12	0.03		
			0.15	0.03		
13.7	7.38	0.70	0.31	0.03	-	-
			0.15	0.03		
			0.21	0.03		
			0.11	0.03		
			0.58	0.03		
			0.27	0.03		
13.8	8.72	0.73	0.31	0.03	-	-
			0.26	0.03		
			0.23	0.03		
			0.16	0.03		
			0.32	0.03		
			0.18	0.03		

Superheat	Heat flux	Absolute uncertainty	Departure diameter	Absolute uncertainty	Departure frequency	Absolute uncertainty
T_w - T_{sat}	q''	$\omega_{q''}$	d_D	ω_{dD}	f	ω_f
°C	W/cm^2	W/cm^2	mm	mm	1/s	1/s
16.7	10.21	0.71	0.15	0.03	-	-
			0.15	0.03		
			0.30	0.03		
			0.15	0.03		
			0.38	0.03		
18.6	12.31	0.72	0.30	0.03	-	-
			0.27	0.03		
			0.17	0.03		
			0.38	0.03		
			0.25	0.03		
			0.25	0.03		
	Average (Nucleate boiling)		0.25	0.05	-	
	Average (Near CHF)[b]		-		-	

[a] Measurements for this condition were excluded
[b] CHF conditions were not reached for this experiment due to equipment failure

APPENDIX B

The formula used for Hsu's hypothesis calculations is

$$\Delta T_{\min} = \frac{4\,\sigma T_{\text{sat}} \sin\,\theta}{\rho_{\,v} h_{fg} D_c} \tag{B1}$$

where D_c is the critical cavity diameter in meters and $\Delta T_{\min}$ is the minimum superheat required to initiate nucleation. For PF-5060 on a CNT-coated surface, we use $\theta = 13°$, $\sigma = 0.0083$ N/m, $T_{\text{sat}} = 329.15$ K, $\rho_v = 13.1493$ kg/m^3, and $h_{fg} = 84711$ J/kg to get $\Delta T_{\min} = 44$ K (for $D_c = 50 \times 10^{-9}$ m), $\Delta T_{\min} = 22$ K (for $D_c = 100 \times 10^{-9}$ m), and $\Delta T_{\min} = 0.55$ K (for $D_c = 4 \times 10^{-6}$ m).

VITA

Name:	Stephen Thomas Glenn
Address:	Department of Mechanical Engineering Texas A&M University College Station, TX, 77843-3123
Email Address:	sglenn06@gmail.com
Education:	B.S., Mechanical Engineering, Texas A&M University, 2006 M.S., Mechanical Engineering, Texas A&M University, 2009